

1 **Examination of aerosol impacts on convective clouds and precipitation in two**
2 **metropolitan areas in East Asia; how varying depths of convective clouds between**
3 **the areas diversify those aerosol effects?**

4

5 Seoung Soo Lee^{1,2}, Jinho Choi³, Goun Kim⁴, Kyung-Ja Ha^{2,5,6}, Kyong-Hwan Seo³, Chang-
6 Hoon Jung⁷, Junshik Um³, Youtong Zheng⁸, Jianping Guo⁹, Sang-Keun Song¹⁰

7

8 ¹Earth System Science Interdisciplinary Center, University of Maryland, Maryland

9 ²Research Center for Climate Sciences, Pusan National University, Busan, Republic of

10 Korea

11 ³Department of Atmospheric Sciences, Division of Earth Environmental System, Pusan

12 National University, Busan, Republic of Korea

13 ⁴Marine Disaster Research Center, Korea Institute of Ocean Science and Technology,

14 Pusan, Republic of Korea

15 ⁵Center for Climate Physics, Institute for Basic Science, Busan, Republic of Korea

16 ⁶BK21 School of Earth and Environmental Systems, Pusan National University, Busan,

17 Republic of Korea

18 ⁷Department of Health Management, Kyungin Women's University, Incheon, Republic of

19 Korea

20 ⁸The Program in Atmospheric and Oceanic Sciences, Princeton University,

21 and National Oceanic and Atmospheric Administration/Geophysical Fluid Dynamics

22 Laboratory, Princeton, New Jersey, USA

23 ⁹State Key Laboratory of Severe Weather, Chinese Academy of Meteorological Sciences,

24 Beijing, China

25 ¹⁰Department of Earth and Marine Sciences, Jeju National University, Jeju, Republic of

26 Korea

27

28 Corresponding author: Seoung Soo Lee

29 Office: (303) 497-6615

30 Fax: (303) 497-5318

31 E-mail: cumulss@gmail.com, slee1247@umd.edu

32

33

34

35

36

37

38

39

40

41

42

43

44

45

46

47

48

49

50

51

52 Abstract

53

54 This study examines the role played by aerosols which act as cloud condensation nuclei
55 (CCN) in the development of clouds and precipitation in two metropolitan areas in East
56 Asia that have experienced substantial increases in aerosol concentrations over the last
57 decades. These two areas are the Seoul and Beijing areas and the examination has been
58 done by performing simulations using the Advanced Research Weather Research and
59 Forecasting model as a cloud-system resolving model. CCN are advected from the
60 continent to the Seoul area and this increases aerosol concentrations in the Seoul area.
61 These increased CCN concentrations induce the enhancement of condensation that in turn
62 induces the enhancement of deposition and precipitation amount in a system of less deep
63 convective clouds as compared to those in the Beijing area. In a system of deeper clouds
64 in the Beijing area, increasing CCN concentrations also enhance condensation but reduce
65 deposition. This leads to CCN-induced negligible changes in precipitation amount. Also,
66 in the system, there is a competition for convective energy among clouds with different
67 condensation and updrafts. This competition results in different responses to increasing
68 CCN concentrations among different types of precipitation, which are light, medium and
69 heavy precipitation in the Beijing area. CCN-induced changes in freezing play a negligible
70 role in CCN-precipitation interactions as compared to the role played by CCN-induced
71 changes in condensation and deposition in both of the areas.

72

73

74

75

76

77

78

79

80

81

82

1. Introduction

83

84

85 With increasing aerosol loading or concentrations, cloud-particle sizes can be changed. In
86 general, with increasing droplet sizes, the efficiency of collision and collection among
87 droplets increases. Increasing aerosol loading is known to make the droplet size smaller
88 and thus make the efficiency of collision and collection among droplets lower. This leads
89 to less droplets or cloud liquid forming raindrops and there is more cloud liquid present in
90 the air to be evaporated or frozen. Studies have shown that increases in cloud-liquid mass
91 due to increasing aerosol loading can enhance the freezing of cloud liquid and parcel
92 buoyancy, which lead to the invigoration of convection (Rosenfeld et al., 2008; Fan et al.,
93 2009). Via the invigoration of convection, precipitation can be enhanced. The dependence
94 of aerosol-induced invigoration of convection and precipitation enhancement on aerosol-
95 induced increases in condensational heating in the warm sector of a cloud system has been
96 shown (e.g., van den Heever et al., 2006; Fan et al., 2009; Lee et al., 2018). Increasing
97 cloud-liquid mass induces increasing evaporation, which intensifies gust fronts. This in
98 turn strengthens convective clouds and increases the amount of precipitation (Khain et al.,
99 2005; Tao et al., 2007; Storer et al., 2010; Tao et al., 2012; Lee et al., 2017; Lee et al.,
100 2018). It is notable that aerosol-induced precipitation enhancement is strongly sensitive to
101 cloud types that can be defined by cloud characteristics such as cloud depth (e.g., Tao et
102 al., 2007; Lee et al., 2008; Fan et al., 2009).

103

104 Since East Asia was industrialized, there have been substantial increases in aerosol
105 concentrations over the last decades in East Asia (e.g., Lee et al., 2013; Lu et al., 2011; Oh
106 et al., 2015; Dong et al., 2019). These increases are far greater than those in other regions
107 such as North America and Europe (e.g., Lu et al., 2011; Dong et al., 2019). While those
108 increasing aerosols affect clouds, precipitation and hydrologic circulations in the
109 continental East Asia, the increase in the advected aerosols from the continent to the
110 Korean Peninsula affect clouds, precipitation and hydrologic circulations in the Korean
111 Peninsula (Kar et al., 2009). This study aims to examine effects of the increasing aerosols,
112 which particularly act as cloud condensation nuclei (CCN), and their advection on clouds
113 and precipitation in East Asia. This study focuses on aerosols which act as CCN, but not
ice-nucleating particles (INPs), to examine those effects, based on the fact that CCN

114 account for most of aerosol mass that affects clouds and precipitation, and CCN, but not
115 INPs, are associated with above-described aerosol-induced invigoration of convection and
116 intensification of gust fronts. Note that these aerosol-induced invigoration and
117 intensification are two well-established major theories of aerosol-cloud interactions. As a
118 first step to the examination, this study focuses on two metropolitan areas in East Asia
119 which are the Beijing and Seoul areas. The population of each of the Beijing and Seoul
120 areas is ~ 20 millions. Associated with this, these areas have lots of aerosol sources (e.g.,
121 traffic) and have made a substantial contribution to the increases in aerosol concentrations
122 in East Asia. Hence, we believe that these two cities can represent overall situations related
123 to increasing aerosol concentrations in East Asia.

124 As mentioned above, aerosol-cloud interactions (and their impacts on precipitation) are
125 strongly dependent on cloud types and thus to gain a more general understanding of those
126 interactions, we select cases from the Beijing and Seoul areas with different cloud types.
127 A selected case from the Beijing area involves deep convective clouds that reach the
128 tropopause, while a selected case from the Seoul area involves comparatively shallow (or
129 less deep) convective clouds. Via comparisons between these two cases, we aim to identify
130 mechanisms that control varying aerosol-cloud interactions with cloud types.

131 To examine impacts of aerosols, which act as CCN, on clouds and precipitation in the
132 cases, numerical simulations are performed, as a way of fulfilling above-described aim.
133 These simulations use a cloud-system resolving model (CSRМ) that has reasonably high
134 resolutions to resolve cloud-scale processes that are related to cloud microphysics and
135 dynamics. Hence, these simulations are able to find process-level mechanisms in
136 association with cloud-scale processes.

137

138 **2. Case description**

139

140 In the Seoul area, South Korea, there is an observed mesoscale convective system (MCS)
141 for a period from 03:00 LST (local solar time) to 18:00 LST December 24th 2017. During
142 this period, there is a recorded moderate amount of precipitation and its maximum
143 precipitation rate reaches ~ 13 mm hr⁻¹. Here, precipitation in the Seoul area is measured
144 by rain gauges in automatic weather stations (AWSs) (King, 2009). The measurement is

145 performed hourly with a spatial resolution that ranges from ~1 km to ~10 km. The Seoul
146 area is marked by an inner rectangle in Figure 1a and dots in the rectangle in Figure 1a
147 mark the selected locations of rain gauges. At 21:00 LST December 23rd 2017, synoptic-
148 scale features develop in favor of the formation and development of the selected MCS and
149 associated moderate rainfall. These features involve the southwesterly low-level jets that
150 transport warm and moist air to the Korean Peninsula. The southwesterly low-level jet
151 plays an important role in the formation and development of rainfall events in the Korean
152 Peninsula by fetching warm and moist air (Hwang and Lee 1993; Lee et al. 1998; Seo et
153 al. 2013; Oh et al. 2018).

154 There was another observed MCS case in the Beijing area, China for a period from
155 14:00 LST on July 27th to 00:00 LST July 28th 2015. There is a substantial recorded amount
156 of precipitation for this period and its maximum precipitation rate reaches ~ 45 mm hr⁻¹.
157 Here, similar to the situation in the Seoul area, precipitation in the Beijing area is measured
158 by rain gauges in AWSs hourly with a spatial resolution that ranges from ~1 km to ~10 km.
159 The Beijing area is marked by an inner rectangle in Figure 1b and dots in the rectangle in
160 Figure 1b mark the selected locations of rain gauges. At 09:00 LST July 27th 2015,
161 synoptic-scale features develop in favor of the formation and development of the selected
162 MCS. These features involve the southerly low-level jet that develops heavy rainfall events
163 in the Beijing area by transporting warm and moist air to the area. Synoptic features which
164 are described here are based on reanalysis data that are produced by the Met Office Unified
165 Model (Brown et al., 2012) every 6 hours with a $0.11^\circ \times 0.11^\circ$ resolution.

166

167 **3. CSRM and simulations**

168

169 **3.1 CSRM**

170

171 The Advanced Research Weather Research and Forecasting (ARW) model (version 3.3.1)
172 is used as a CSRM. The ARW model is a compressible model with a nonhydrostatic status.
173 A 5th-order monotonic advection scheme is used to advect microphysical variables (Wang
174 et al., 2009). The Rapid Radiation Transfer Model (RRTMG; Mlawer et al., 1997; Fouquart
175 and Bonnel, 1980) is adopted to parameterize shortwave and longwave radiation in

176 simulations. A microphysics scheme that is used in this study calculates the effective sizes
177 of hydrometeors that are fed into the RRTMG, and the RRTMG simulates how these
178 effective sizes affect radiation.

179 The CSRМ adopts a bin scheme as a way of parameterizing microphysics. The
180 Hebrew University Cloud Model (HUCM) detailed in Khain et al. (2011) is the bin scheme.
181 A set of kinetic equations is solved by the bin scheme to represent a size distribution
182 function for each of seven classes of hydrometeors and aerosols acting as CCN. Hence,
183 there are seven size distribution functions for hydrometeors. The seven classes of
184 hydrometeors are water drops, three types of ice crystals, which are plates, columns and
185 dendrites, snow aggregates, graupel and hail. Drops whose radius is smaller (larger) than
186 40 μm are categorized to be droplets (raindrops). There are 33 bins for each size
187 distribution in a way that the mass of a particle m_j in the j bin is to be $m_j = 2m_{j-1}$.

188 A cloud-droplet nucleation parameterization based on Köhler theory represents cloud-
189 droplet nucleation. Arbitrary aerosol mixing states and aerosol size distributions can be fed
190 to this parameterization. To represent heterogeneous ice-crystal nucleation,
191 parameterizations by Lohmann and Diehl (2006) and Möhler et al. (2006) are used. In these
192 parameterizations, contact, immersion, condensation-freezing, and deposition nucleation
193 paths are all considered by taking into account the size distribution of INPs, temperature
194 and supersaturation. Homogeneous droplet freezing is
195 considered following the theory developed by Koop et al. (2000).

196

197 **3.2 Control runs**

198

199 For a three-dimensional CSRМ simulation of the observed case of convective clouds in the
200 Seoul (Beijing) area, i.e., the control-s (control-b) run, a domain just over the Seoul
201 (Beijing) area, which is shown in Figure 1a (1b), is used. This domain adopts a 300-m
202 resolution. The control-s run is for a period from 03:00 LST to 18:00 LST December 24th
203 2017, while the control-b run is for a period from 14:00 LST on July 27th to 00:00 LST
204 July 28th 2015. The length of the domain is 170 (140) km in the east-west (north-south)
205 direction for the control-s run, and 280 (240) km for the control-b run. There are 100
206 vertical layers and these layers employ a sigma coordinate that follows the terrain. The top

207 pressure of the model is 50 hPa for both of the control-s and control-b runs. On average,
208 the vertical resolution is ~200 m.

209 Reanalysis data, which are produced by the Met Office Unified Model (Brown et al.,
210 2012), represent the synoptic-scale features, provide initial and boundary conditions of
211 variables such as wind, potential temperature, and specific humidity for the simulations.
212 The simulations adopt an open lateral boundary condition. The Noah land surface model
213 (LSM; Chen and Dudhia, 2001) calculates surface heat fluxes.

214 The current version of the ARW model is not able to consider the spatiotemporal
215 variation of aerosol properties. In order to take into account the spatiotemporal variation of
216 aerosol properties, which is typical in metropolitan areas, such as composition and number
217 concentration, an aerosol preprocessor, which is able to consider the variability of aerosol
218 properties, is developed and used in the simulations. This aerosol preprocessor interpolates
219 or extrapolates background aerosol properties in observation data such as aerosol mass
220 (e.g., PM_{2.5} and PM₁₀) into grid points and time steps in the model. In this study, the inverse
221 distance weighting method is used for the extrapolation and interpolation of observation
222 data including aerosol mass into grid points and time steps in the model. PM stands for
223 particulate matter. The mass of aerosols with diameter smaller than 2.5 (10.0) μm per unit
224 volume of the air is PM_{2.5} (PM₁₀).

225 There are surface observation sites, which measure aerosol properties, in the domains
226 and these sites are classified into two types; the selected locations of these sites are marked
227 by dots in the inner rectangles in Figure 1. The distance between the observation sites
228 ranges from ~1 km to ~10 km and the time interval between observations is ~10 minutes.
229 More than 90% of the sites belong to the first type of the sites. These first-type sites are
230 managed by the government in South Korea or China, and measure PM_{2.5} or PM₁₀ but not
231 other aerosol properties such as aerosol composition and size distributions. Less than 10%
232 of the sites belong to the second type of the sites. These second-type sites are a part of
233 aerosol robotic network (AERONET; Holben et al., 2001) and measure aerosol
234 composition and size distributions. The production of aerosol data in these second-type or
235 AERONET sites is viable only in the presence of the sun. The first-type sites observe PM_{2.5}
236 or PM₁₀ using the beta-ray attenuation method (Eun et al., 2016; Ha et al., 2019) and hence,
237 produce PM_{2.5} or PM₁₀ data whether the sun is present or not. PM_{2.5}/PM₁₀ data from the

238 first-type sites are used to represent the spatiotemporal variability of aerosols over the
239 domains and the simulation periods. To represent aerosol composition and size
240 distributions, data from the AERONET sites are employed.

241 The AERONET data are averaged over the AERONET sites at 02:00 LST December
242 24th 2017 (13:00 LST July 27th 2015), which is 1 hour before the observed MCS forms, for
243 the Seoul (Beijing) case. Based on the average data, it is assumed that aerosol particles are
244 internally mixed with 70 (80) % ammonium sulfate and 30 (20) % organic compound for
245 the Seoul (Beijing) case. This mixture is assumed to represent aerosol chemical
246 composition in the whole domain and during the entire simulation period. Since ammonium
247 sulfate and organic compound are representative components of CCN, it is assumed that
248 PM_{2.5} and PM₁₀, which are from the first-type sites, represent the mass of aerosols that act
249 as CCN for the Seoul and Beijing areas, respectively. Aerosols reflect, scatter and absorb
250 shortwave and longwave radiation before they are activated. This type of aerosol-radiation
251 interactions is not taken into account in this study. This is mainly based on the fact that in
252 the mixture, there is insignificant amount of radiation absorbers; black carbon is a
253 representative radiation absorber. The average AERONET data indicate that the size
254 distribution of background aerosols acting as CCN follows the bi-modal log-normal
255 distribution for both of the Seoul and Beijing cases. Based on the average AERONET data,
256 it is assumed that for the whole domain and simulation period, the size distribution of
257 background aerosols acting as CCN follows a shape of distribution with specific size
258 distribution parameters (i.e., modal radius and standard deviation of each of accumulation
259 and coarse modes, and the partition of aerosol number among those modes) for each of the
260 cases. Modal radius of the shape of distribution is 0.110 (0.085) and 1.413 (1.523) μm ,
261 while standard deviation of the shape of distribution is 1.54 (1.63) and 1.75 (1.73) for
262 accumulation and coarse modes, respectively, in the Seoul (Beijing) case. The partition of
263 aerosol number, which is normalized by the total aerosol number of the size distribution,
264 is 0.999 and 0.001 for accumulation and coarse modes, respectively, in both of the cases.
265 By using PM_{2.5} or PM₁₀, which is not only from the first-type sites but also interpolated
266 and extrapolated to grid points immediately above the surface and time steps, and based on
267 the assumption of aerosol composition and size distribution above, which is in turn based
268 on data from the AERONET sites, the background number concentrations of aerosols

269 acting as CCN are obtained for the simulation for each of the cases. There is no variation
270 with height in background concentrations of aerosols acting as CCN from immediately
271 above the surface to the top of the planetary boundary layer (PBL). However, it is assumed
272 that they decrease exponentially with height from the PBL top upward. With this
273 exponential decrease, when the altitude reaches the tropopause, background concentrations
274 of aerosols acting as CCN reduce by a factor of ~ 10 as compared to those at the PBL top.
275 The size distribution and composition of aerosols acting as CCN do not vary with height.
276 Once background aerosol properties (i.e., aerosol number concentrations, size distribution
277 and composition) are put into each grid point and time step, those properties at each grid
278 point and time step do not change during the course of the simulations.

279 For the control-s and control-b runs, aerosol properties of INPs are not different from
280 those of CCN except for the fact that the concentration of background aerosols acting as
281 CCN is 100 times higher than the concentration of background aerosols acting as INPs at
282 each time step and grid point, following a general difference between CCN and INPs in
283 terms of their concentrations (Pruppacher and Klett, 1978).

284 Once clouds form and background aerosols start to be in clouds, those aerosols are
285 not background aerosols anymore and the size distribution and concentrations of those
286 aerosols begin to evolve through aerosol sinks and sources that include advection and
287 aerosol activation (Fan et al., 2009). For example, once aerosols are activated, they are
288 removed from the corresponding bins of the aerosol spectra. In clouds, after aerosol
289 activation, aerosol mass starts to be inside hydrometeors and via collision-collection, it
290 transfers to different types and sizes of hydrometeors. In the end, aerosol mass disappears
291 in the atmosphere when hydrometeors with aerosol mass touches the surface. In non-cloudy
292 areas, aerosol size and spatial distributions are designed to be identical to the size and
293 spatial distributions of background aerosols, respectively. In other words, for this study,
294 we use “the aerosol recovery method”. In this method, at any grid points, immediately after
295 clouds disappear entirely, aerosol size distributions and number concentrations recover to
296 background properties that background aerosols at those points have before those points
297 are included in clouds. In this way, we can keep concentrations of background aerosols
298 outside clouds in the simulations at observed counterparts. This enables spatiotemporal
299 distributions of background aerosols in the simulations to mimic those distributions that

300 are observed and particularly associated with observed aerosol advection in reality. In the
301 aerosol recovery method, there is no time interval between the cloud disappearance and the
302 aerosol recovery. Here, when the sum of mass of all types of hydrometeors (i.e., water
303 drops, ice crystals, snow aggregates, graupel and hail) is not zero at a grid point, that grid
304 point is considered to be in clouds. When this sum becomes zero, clouds are considered to
305 disappear. Many studies using CSRM have employed this aerosol recovery method. They
306 have proven that with the recovery method, reasonable simulations of overall cloud and
307 precipitation properties are accomplished (e.g., Morrison and Grabowski, 2011; Lebo and
308 Morrison, 2014; Lee et al., 2016; Lee et al., 2018).

309

310 **3.3 Additional runs**

311

312 We repeat the control-s run by getting rid of aerosol-advection induced increases in
313 concentrations of aerosols acting as CCN as a way of investigating how the aerosol
314 advection affects the cloud system in the Seoul area. This repeated run is named the low-
315 aerosol-s run. An aerosol layer, which is advected from East Asia or from the west of the
316 Seoul area to it, increases aerosol concentrations in the Seoul area. There are stations in
317 islands in the Yellow Sea that monitor the aerosol advection (Eun et al., 2016; Ha et al.,
318 2019). To monitor and identify the aerosol advection, $PM_{2.5}$ which is measured by a station
319 in Baekryongdo island in Yellow Sea are compared to those which are measured in stations
320 in and around the Seoul area. In Figure 1a, a dot outside the inner rectangle marks the
321 island. The time evolution of $PM_{2.5}$ measured by the station on the island and the average
322 $PM_{2.5}$ over stations in the Seoul area, between 07:00 LST on December 22nd and 21:00 LST
323 on December 24th in 2017 when there is the strong advection of aerosols from East Asia to
324 the Seoul area, is shown in Figure 2. At 09:00 LST on December 22nd, the advection of
325 aerosols from East Asia enables aerosol mass to start going up and attain its peak around
326 05:00 LST on December 23rd on the island. Following this, aerosol mass starts to increase
327 in the Seoul area around 01:00 LST on December 23rd, and the mass attains its peak at
328 15:00 LST on December 23rd in the Seoul area. This is because aerosols, which are
329 advected from East Asia, move through the island to reach the Seoul area.

330 In the low-aerosol-s run, as a way of getting rid of aerosol-advection induced increases
331 in concentrations of aerosols acting as CCN, it is assumed that $PM_{2.5}$, which is assumed to
332 represent the mass of aerosols acting as CCN, and the associated background concentration
333 of aerosols acting as CCN after 01:00 LST on December 23rd do not evolve with the aerosol
334 advection in the Seoul area. Hence, the background concentration of aerosols acting as
335 CCN is assumed to have that at 01:00 LST on December 23rd at each time step and grid
336 point at the beginning of the simulation period. However, to isolate CCN effects on clouds,
337 background aerosol concentration acting as INPs at each time step and grid point in the
338 low-aerosol-s run is not different from that in the control-s run during the simulation period.
339 In the observed PM data for the Seoul area, there is reduction in PM by a factor of ~ 10 on
340 average over a period between $\sim 07:00$ and $\sim 14:00$ LST on December 24th, since
341 precipitation scavenges aerosols (Figure 2). To emulate this scavenging and reflect it in
342 background aerosols acting as CCN for the low-aerosol-s run, $PM_{2.5}$ and corresponding
343 background concentrations of aerosols acting as CCN at each grid point is gradually
344 reduced for the period between 07:00 and 14:00 LST on December 24th. This reduction is
345 done in a way that background concentrations of aerosols acting as CCN at each grid point
346 at 14:00 LST on December 24th is 10 times lower than that at 07:00 LST on December 24th
347 in the low-aerosol-s run. Then, $PM_{2.5}$ and corresponding background concentrations of
348 aerosols acting as CCN at each grid point at 14:00 LST on December 24th maintains until
349 the end of the simulation period. This results in the evolution of the average $PM_{2.5}$ over the
350 Seoul area in the low-aerosol-s run as shown in Figure 2. Here, the concentration of
351 background aerosols acting as CCN, which is averaged over the whole domain and
352 simulation period, in the control-s run is 3.1 times higher than that in the low-aerosol-s run.
353 Via comparisons between the runs, how the increasing concentration of background
354 aerosols acting as CCN due to the aerosol advection has an impact on clouds can be
355 examined. The concentration of background aerosols acting as CCN is different among
356 grid points and time steps in the control-s run. Hence, the ratio of the concentration of
357 background aerosols acting as CCN between the runs is different among grid points and
358 time steps.

359 For the Beijing case, to examine how aerosols acting as CCN affect clouds and
360 precipitation, we repeat the control-b run with simply reduced concentrations of

361 background aerosols acting as CCN at each time step and grid point by a factor of 3.1. This
362 repeated run is named the low-aerosol-b run. The 3.1-fold increase in aerosol
363 concentrations from the low-aerosol-b run to the control-b is based on the 3.1-fold increase
364 in the average concentration of background aerosols acting as CCN from the low-aerosol-
365 s run to the control-s run. However, as in the control-s and low-aerosol-s runs, to isolate
366 CCN effects on clouds, background aerosol concentration acting as INPs at each time step
367 and grid point in the low-aerosol-b run is identical to that in the control-b run during the
368 simulation period. Hence, on average, a pair of the control-s and low-aerosol-s runs has the
369 same perturbation of aerosols acting as CCN as in a pair of the control-b and low-aerosol-
370 b runs. Here, we define aerosol perturbation as a relative increase in aerosol concentration
371 when compared to that before the increase occurs. The brief summary of all simulations in
372 this study is given in Table 1.

373

374 **4. Results**

375

376 **4.1 Cumulative precipitation**

377

378 We compare the observed precipitation to the simulated counterpart in the control-s run for
379 the Seoul case and in the control-b run for the Beijing case. For this comparison, the
380 observed and simulated precipitation rates at the surface are averaged over the domain for
381 each of the Seoul and Beijing cases (Figures 3a and 3b). Here, the simulated precipitation
382 rates are smoothed over 1 hour. The comparison shows that the evolution of the simulated
383 precipitation rate does not deviate from the observed counterpart significantly (Figures 3a
384 and 3b).

385 In the Seoul case, overall, the precipitation rate is higher in the control-s run than in
386 the low-aerosol-s run. As a result of this, the domain-averaged cumulative precipitation
387 amount at the last time step is 14.1 mm and 12.0 mm in the control-s run and the low-
388 aerosol-s run, respectively. The control-s run shows ~20 % higher cumulative precipitation
389 amount. In the Beijing case, the evolution of the mean precipitation rate in the control-b
390 run is not significantly different from that in the low-aerosol-b run. Due to this, the control-
391 b run shows only ~2 % higher cumulative precipitation amount, despite the fact that the

392 concentrations of background aerosols acting as CCN are ~ 3 times higher in the control-b
393 run than in the low-aerosol-b run. Note that in the Seoul case, the time- and domain-
394 averaged concentration of background aerosols acting as CCN is also ~ 3 times higher in
395 the control-s run than in the low-aerosol-s run. Despite this, the difference in the cumulative
396 precipitation amount between the runs with different concentrations of background
397 aerosols acting as CCN is greater in the Seoul case than in the Beijing case.

398

399 **4.2 Precipitation, and associated latent-heat and dynamic processes**

400

401 Figures 4a and 4b show the cumulative frequency distributions of precipitation rates at the
402 last time step in the simulations for the Seoul and Beijing cases, respectively. In each of
403 those figures, the observed frequency distribution is shown and compared to the simulated
404 distribution. The observed distribution is obtained by interpolating and extrapolating the
405 observed precipitation rates to grid points and time steps in each of the control-s and
406 control-b runs. The observed maximum precipitation rates are 13.0 and 44.5 mm hr⁻¹ for
407 the Seoul and Beijing cases, respectively, and these maximum rates are similar to those in
408 the control-s and control-b runs, respectively. Overall, the observed and simulated
409 frequency distributions are in good agreement for each of the cases. This enables us to
410 assume that results in the control-s (control-b) run are benchmark results to which results
411 in the low-aerosol-s (low-aerosol-b) run can be compared to identify how aerosols acting
412 as CCN have an impact on clouds and precipitation for the Seoul (Beijing) case. Here, it is
413 notable that for the Beijing case, while differences in the cumulative precipitation amount
414 between the control-b and low-aerosol-b runs are not significant, features in the frequency
415 distribution of precipitation rates between those runs are substantially different (Figure 4b).

416

417 **1) Seoul case**

418

419 **a. Precipitation Frequency distributions**

420

421 Regarding precipitation whose rates are higher than ~ 2 mm hr⁻¹, the cumulative
422 precipitation frequency at the last time step is higher in the control-s run as compared to

423 that in the low-aerosol-s run (Figure 4a). In particular, for the precipitation rate of 11.4 mm
424 h^{-1} , there is an increase in the cumulative frequency by a factor of as much as ~ 10 in the
425 control-s run. When it comes to precipitation rates above 11.5 mm hr^{-1} , precipitation is
426 present in the control-s run and precipitation is absent in the low-aerosol-s run. Regarding
427 precipitation whose rates are lower than $\sim 2 \text{ mm hr}^{-1}$, differences in the cumulative
428 frequency between the runs are insignificant. Hence, we see that there are significant
429 increases in the frequency of relatively heavy precipitation whose rates are above $\sim 2 \text{ mm}$
430 hr^{-1} in the control-s run when compared to that in the low-aerosol-s run. At the last time
431 step, this results in a larger amount of cumulative precipitation in the control-s run than in
432 the low-aerosol-s run.

433 The time evolution of the cumulative precipitation frequency is shown in Figure 5. At
434 06:00 LST December 24th 2017, which corresponds to the initial stage of the precipitation
435 development, the maximum precipitation rate reaches $\sim 3 \text{ mm hr}^{-1}$ and there is the greater
436 frequency over most of precipitation rates in the control-s run than in the low-aerosol-s run
437 (Figure 5a). With the time progress from 06:00 LST to 10:00 LST, the maximum
438 precipitation rate increases to reach 12 mm hr^{-1} and the cumulative frequency is higher over
439 precipitation whose rates are higher than $\sim 3 \text{ mm hr}^{-1}$ in the control-s run, while for
440 precipitation whose rates are lower than $\sim 3 \text{ mm hr}^{-1}$, differences in the cumulative
441 frequency between the runs are negligible (Figures 5a and 5b). When time reaches 12:00
442 LST, which is around time when the peak in the evolution of the area-averaged
443 precipitation rates occurs and thus the system is at its mature stage, the maximum
444 precipitation rate increases up to $\sim 13 \text{ mm hr}^{-1}$ (Figures 3a and 5c). The basic patterns of
445 differences in the cumulative precipitation frequency between the runs with the maximum
446 precipitation rate around 13 mm hr^{-1} , which are established at 12:00 LST, maintain until
447 the end of the simulation period (Figures 4a and 5c).

448

449 **b. Condensation, deposition, updrafts and associated variables**

450

451 Note that the source of precipitation is precipitable hydrometeors which are raindrops,
452 snow, graupel and hail particles. Droplets and ice crystals are the source of those
453 precipitable hydrometeors mostly via collision and coalescence processes. Droplets and ice

454 crystals gain their mass mostly via condensation and deposition. Based on this, to explain
455 the greater cumulative precipitation amount in the control-s run than in the low-aerosol-s
456 run, the evolutions of differences in condensation, deposition and associated updrafts
457 between the runs are analyzed. The vertical profiles of differences in the area-averaged
458 condensation, deposition and freezing rates, updraft mass fluxes and the associated mass
459 density of each class of hydrometeors between the runs at 03:20, 03:40, 06:00 and 12:00
460 LST are shown in Figure 6. In Figure 6, differences in freezing rates are added for a more
461 comprehensive understanding of processes that are related to differences in cumulative
462 precipitation amount between the runs. Freezing includes riming processes between liquid
463 and solid hydrometeors and these riming processes act as a source of precipitable
464 hydrometeors. Cloud fractions are 0.32 (0.30), 0.85 (0.82), 0.93 (0.92) and 1.00 (1.00) in
465 the control-s (low-aerosol-s) run at 03:20, 03:40, 06:00 and 12:00 LST, respectively. We
466 see that cloud fraction varies 0~6% between the runs. Note that in all of figures, which
467 display snow and hail mass density and include Figure 6, snow mass density includes ice-
468 crystal mass density, while hail mass density includes graupel mass density for the sake of
469 the display brevity. In Figure 6, horizontal black lines represent the altitudes of freezing
470 and melting.

471 Condensation rates in the control-s run start to be larger than that in the low-aerosol-
472 s run at 03:20 LST (Figure 6a). Higher aerosol or CCN concentrations induce more
473 nucleation of droplets, higher cloud droplet number concentration (CDNC) and associated
474 greater integrated surface of droplets in the control-s run. CDNC, which is averaged over
475 grid points and time steps with non-zero CDNC, is 1050 and 352 cm^{-3} in the control-s and
476 low-aerosol-s runs, respectively. Hence, more droplet surface is provided for water vapor
477 to condense onto in the control-s run. This leads to more condensation in the control-s run.
478 This establishes stronger feedbacks between updrafts and condensation, leading to greater
479 droplet (or cloud-liquid) mass at 03:20 LST in the control-s run (Figure 6a). Then, these
480 stronger feedbacks, which involve stronger updrafts particularly above 2 km in altitude,
481 subsequently induce greater deposition and snow mass as time progresses from 03:20 LST
482 to 03:40 LST, while more condensation and greater droplet mass maintain in the control-s
483 run with the time progress to 03:40 LST (Figure 6b). These stronger updrafts enable clouds
484 to grow higher in the control-s run. This eventually leads to a situation where the maximum

485 cloud depth is ~ 7 km in the control-s run and this depth is ~ 5 % deeper than that in the low-
486 aerosol-s run for the whole simulation period.

487 Through aerosol-induced stronger feedbacks between condensation, deposition and
488 updrafts in the control-s run, while more condensation and more overall deposition
489 maintain in the control-s run, differences in condensation and deposition between the
490 control-s and low-aerosol-s runs increase as time progresses from 03:40 LST to 06:00 LST
491 (Figures 6b and 6c). Associated with this, the greater mass of raindrops and hail particles
492 appears up, while the greater mass of droplets and snow in the control-s run than in the
493 low-aerosol-s run maintains with the time progress from 03:40 LST to 06:00 LST (Figure
494 6c). At 06:00 LST, there is more freezing starting to occur in the control-s run than in the
495 low-aerosol-s run. However, differences in freezing are \sim one and \sim two orders of magnitude
496 smaller than those in deposition and condensation, respectively. After 06:00 LST until time
497 reaches 12:00 LST when the overall differences in the cumulative precipitation frequency
498 between the runs are established, differences in freezing become ~ 3 times smaller than
499 those in deposition and \sim one order of magnitude smaller than those in condensation
500 (Figures 6c and 6d). The greater mass of hydrometeors in the control-s run also continues
501 after 06:00 LST until time reaches 12:00 LST (Figures 6c and 6d). At 12:00 LST,
502 condensation, deposition and freezing rates are still higher in the control-s run. Here, we
503 see that CCN-induced more cumulative precipitation amount and associated differences in
504 the precipitation frequency distribution between the control-s and low-aerosol-s runs are
505 primarily associated with CCN-induced more condensation, which induce CCN-induced
506 more deposition and higher mass density of hydrometeors as sources of precipitation, but
507 weakly connected to CCN-induced changes in freezing. This is supported by the fact that
508 the time- and domain-averaged differences in freezing rate are \sim one to \sim two order of
509 magnitude smaller than those in condensation and deposition rates.

510

511 **c. Condensation frequency distributions and horizontal distributions of** 512 **condensation and precipitation**

513

514 Based on the importance of condensation for CCN-induced changes in precipitation, the
515 horizontal distribution of the column-averaged condensation rates over the domain and the

516 cumulative frequency distribution of the column-averaged condensation rates at each time
517 step is obtained. To better visualize the role of condensation in precipitation, the horizontal
518 distribution of the column-averaged condensation rates is superimposed on that of
519 precipitation rates (Figure 7). At 03:40 LST, condensation mainly occurs around the
520 northern part of the domain as marked by a yellow rectangle. The synoptic wind condition
521 in the marked area favors the collision between northward and southward wind and the
522 associated convergence around the surface (Figures 7a and 7b). This convergence induces
523 updrafts and condensation in the marked area. In the marked area, more aerosols acting as
524 CCN induce more and more extensive condensation, which leads to the higher domain-
525 averaged condensation rates in the control-s run than in the low-aerosol-s run (Figures 6b,
526 7a and 7b). More droplets are formed on more aerosols acting as CCN and more droplets
527 provide more surface areas where condensation occurs and this enables more and more
528 extensive condensation in the control-s run than in the low-aerosol-s run (Figures 6b, 7a
529 and 7b).

530 At 06:20 LST, a precipitating system is advected into the domain via the western
531 boundary, and as seen in Figures 7c and 7d for 08:40 LST, as time progresses to 08:40 LST,
532 the advected precipitating system is further advected to the east and extended mostly over
533 areas in the northern part of the domain where condensation mainly occurs. This confirms
534 that condensation is the main source of cloud mass and precipitation. In the eastern part of
535 the domain, there are mountains and in particular, higher mountains are on the northeastern
536 part of the domain than in the other parts of the domain. These higher mountains induce
537 forced convection and associated condensation more effectively in the northeastern part
538 than in the other parts. This is in favor of the precipitating system that extends further to
539 the east in the northern part of the domain. Due to more aerosols acting as CCN,
540 condensation, which is induced by forced convection over mountains, is more and more
541 extensive in the control-s run (Figures 7c and 7d). In association with this, there is more
542 extension of the precipitating system in the control-s run than in the low-aerosol-s run. This
543 enables the system in the control-s run to reach the eastern boundary at 08:40 LST, which
544 is earlier than in the low-aerosol-s run (Figures 7c and 7d). The system in the low-aerosol-
545 s run reaches the eastern boundary at 09:00 LST. Here, we see that although aerosols acting
546 as CCN do not change overall locations of the precipitation system, they affect how fast

547 the system extends to the east by affecting the amount of condensation which is produced
548 by forced convection. Associated with this, as seen in Figure 8, the control-s run has the
549 much higher cumulative condensation frequency than the low-aerosol-s run over all of
550 condensation rates during the period between 07:20 and 09:00 LST. Contributed by this,
551 the higher precipitation frequency over most of precipitation rates occurs in the control-s
552 run during and after the period (Supplementary Figures 1a and 1b and Figures 5b and 5c).

553 At 10:00 LST, in the southern part of the domain, there is a precipitating area forming
554 as marked by a yellow rectangle (Figures 7e and 7f). The precipitation area in the southern
555 part of the domain extends and merges into the advecting main precipitating system in the
556 northern part of the domain. The merge leads to precipitation that occupies most of the
557 domain at 12:00 LST (Figures 7g and 7h). After 10:00 LST, associated with this merge,
558 the maximum precipitation rate increases to 13 mm hr^{-1} at 12:00 LST (Figures 5c). After
559 13:00 LST, the precipitation enters its dissipating stage and its area reduces and nearly
560 disappears. Even after the merge, CCN-induced more condensation maintains and this in
561 turn contributes to a situation where the control-s run has the greater precipitation
562 frequency over most of precipitation rates than in the low-aerosol-s run until the
563 simulations progress to their last time step (Figures 4a, 5c and 6d).

564

565 **2) Beijing case**

566

567 Stronger convection and deeper clouds develop in the Beijing case than in the Seoul case.
568 The maximum cloud depth is ~ 7 and ~ 12 km in the control-s and control-b runs,
569 respectively. In the Seoul case, clouds do not reach the tropopause, while they reach the
570 tropopause in the Beijing case. Deeper clouds in the Beijing case produce the maximum
571 precipitation rate of $\sim 45 \text{ mm hr}^{-1}$ in the control-b run. However, less deep clouds in the
572 Seoul case produce the maximum precipitation rate of $\sim 13 \text{ mm hr}^{-1}$ in the control-s run
573 (Figure 4).

574

575 **a. Precipitation frequency distributions**

576

577 When it comes to precipitation whose rates are higher than $\sim 12 \text{ mm hr}^{-1}$, the control-b run
578 has the higher cumulative precipitation frequency at the last time step than the low-aerosol-
579 b run (Figure 4b). Particularly, for the precipitation rates of 28.1 and 30.0 mm hr^{-1} , the
580 cumulative frequency increases by a factor of as much as ~ 10 . Moreover, regarding
581 precipitation rates higher than $\sim 33 \text{ mm hr}^{-1}$, precipitation is present in the control-b run,
582 however, precipitation is absent in the low-aerosol-b run. Hence, we see that the frequency
583 of comparatively heavy precipitation whose rates are higher than $\sim 12 \text{ mm hr}^{-1}$ rises
584 significantly in the control-b run as compared to that in the low-aerosol-b run. Below ~ 2
585 mm hr^{-1} , there is also the greater precipitation frequency in the control-b run than in the
586 low-aerosol-b run. Unlike the situation for precipitation rates above $\sim 12 \text{ mm hr}^{-1}$ and below
587 $\sim 2 \text{ mm hr}^{-1}$, for precipitation rates from $\sim 2 \text{ mm hr}^{-1}$ to $\sim 12 \text{ mm hr}^{-1}$, the control-aerosol-b
588 run has the lower precipitation frequency than in the low-aerosol-b run. Here, we see that
589 the higher precipitation frequency above $\sim 12 \text{ mm hr}^{-1}$ and below $\sim 2 \text{ mm hr}^{-1}$ balances out
590 the lower precipitation frequency between ~ 2 and $\sim 12 \text{ mm hr}^{-1}$ in the control-b run. This
591 results in the similar cumulative precipitation amount between the runs.

592 Figure 9 shows the time evolution of the cumulative precipitation frequency. When
593 precipitation starts around 16:00 LST, the higher precipitation frequency occurs over most
594 of precipitation rates in the low-aerosol-run-b run than in the control-b run (Figure 9a). At
595 16:00 LST, the maximum precipitation rate is lower than 1.0 mm hr^{-1} for both of the runs.
596 As time progresses to 17:00 LST, the maximum precipitation rate increases to $\sim 17 \text{ mm hr}^{-1}$
597 and the higher (lower) cumulative precipitation frequency over precipitation rates higher
598 than $\sim 12 \text{ mm hr}^{-1}$ (between ~ 2 and $\sim 12 \text{ mm hr}^{-1}$) in the control-b run than in the low-
599 aerosol-b run, which is described above as shown in Figure 4b for the last time step, starts
600 to emerge (Figure 9b). At 17:20 LST, the higher frequency for precipitation rates below 2
601 mm hr^{-1} in the control-b run, which is also described above as shown in Figure 4b for the
602 last time step, starts to show up, while the higher (lower) frequency for precipitation rates
603 higher than $\sim 12 \text{ mm hr}^{-1}$ (between ~ 2 and $\sim 12 \text{ mm hr}^{-1}$) in the control-b run, which is
604 established at 17:00 LST, maintains as time progresses from 17:00 LST to 17:20 LST
605 (Figure 9c). At 17:20 LST, the maximum precipitation rate increases to 42 (19) mm hr^{-1} in
606 the control-b (low-aerosol-b) run (Figure 9c). At 19:00 LST, the maximum precipitation
607 rate increases to ~ 45 (33) mm hr^{-1} for the control-b (low-aerosol-b) run, while the

608 qualitative nature of differences in the precipitation frequency distributions with the tipping
609 precipitation rates of ~ 2 and ~ 12 mm hr⁻¹ between the runs does not vary much between
610 17:20 and 19:00 LST (Figures 9c and 9d). The qualitative nature of differences in the
611 cumulative precipitation frequency between the runs and the maximum precipitation rates
612 in each of the runs, which are established at 19:00 LST, do not vary significantly until the
613 end of the simulation period (Figures 4b and 9d).

614

615 **b. Condensation, deposition, updrafts and associated variables**

616

617 As done for the Seoul case, as a way of better understanding differences in the cumulative
618 precipitation amount and frequency between the control-b and low-aerosol-b runs, the
619 evolutions of differences in the vertical distributions of the area-averaged condensation
620 rates, deposition rates, freezing rates, the mass density of each class of hydrometeors and
621 updrafts mass fluxes are obtained and shown in Figures 10. Cloud fractions are 0.12 (0.11),
622 0.25 (0.22), 0.36 (0.32), 0.43 (0.40) and 0.48 (0.47) in the control-b (low-aerosol-b) run at
623 14:20, 15:40, 16:00, 17:20 and 19:00 LST, respectively. Here, we see that cloud fraction
624 varies by ~ 2 -12% between the runs. In Figure 10, horizontal black lines represent the
625 altitudes of freezing and melting. As seen in Figure 3b, precipitation starts around 16:00
626 LST but differences in condensation rates start at 14:20 LST with higher condensation rates
627 in the control-b run (Figure 10a). Similar to the situation in the Seoul case, higher
628 concentrations of aerosols acting as CCN induce more nucleation of droplets, higher
629 CDNC and associated greater integrated surface of droplets in the control-b run. CDNC,
630 which is averaged over grid points and time steps with non-zero CDNC, is 992 and 341
631 cm⁻³ in the control-b and low-aerosol-b runs, respectively. Hence, more droplet surface is
632 provided for water vapor to condense onto in the control-b run. This leads to more
633 condensation in the control-b run. Due to this, cloud-liquid or droplet mass becomes greater
634 in the control-b run at 14:20 LST (Figure 10a). Increased condensation rates induce
635 increased condensational heating and thus intensified updrafts (Figure 10a). These
636 updrafts enable the maximum cloud depth to be ~ 12 km in the control-b run and this depth
637 is just ~ 1 % deeper than that in the low-aerosol-b run for the whole simulation period. This
638 negligible difference in the maximum cloud depth between the runs is due to the fact that

639 clouds with the maximum depth reach the tropopause in both of runs and thus there is not
640 much wiggle room to make significant differences in cloud depth between the runs.

641 When time reaches 15:40 LST, deposition rates and snow mass start to show
642 differences between the runs, while higher condensation rates and droplet mass maintain
643 in the control-b run with the time progress from 14:20 LST to 15:40 LST. However, unlike
644 the situation in the Seoul case, higher concentrations of aerosols acting as CCN result in
645 lower deposition rates and snow mass in the control-b run (Figure 10b). When time
646 progresses from 15:40 LST to 16:00 LST, differences in freezing start to occur and freezing
647 rates are lower (higher) at altitudes between ~ 6 and ~ 8 km (~ 4 and ~ 6 km), while higher
648 condensation rates and droplet mass, and lower snow mass maintain in the control-b run
649 (Figure 10c). Due to stronger updrafts, which are mainly ascribed to more condensation,
650 deposition rates start to be higher at altitudes between ~ 7 and ~ 9 km and freezing rates are
651 higher at altitudes between ~ 4 and ~ 6 km in the control-b run with the time progress from
652 15:40 LST to 16:00 LST (Figure 10c). Differences in freezing rates are similar to those in
653 deposition and \sim two orders of magnitude smaller than those in condensation at 16:00 LST
654 (Figure 10c). At 16:00 LST, differences in hail mass between the runs appear up and hail
655 mass is slightly lower in the control-b run (Figure 10c). At 17:20 LST, overall, freezing
656 rates are lower at altitudes between ~ 4 and ~ 8 km, while overall, snow and hail mass is still
657 lower, and droplet mass is still higher in the control-b run (Figure 10d). Differences in
658 freezing rates are ~ 2 times smaller than those in deposition and \sim one order of magnitude
659 smaller than those in condensation at 17:20 LST (Figure 10d). Due to more condensation
660 and droplet mass, greater raindrop mass appears up in the control-b run at 17:20 LST
661 (Figure 10d). As the time progresses to 19:00 LST, deposition rates become lower at the
662 altitudes from ~ 7 km to ~ 12 km and overall freezing rates become higher at altitudes from
663 ~ 4 km to ~ 10 km in the control-b run (Figure 10e). Overall, lower snow and hail mass
664 maintains in the control-b run as time progresses from 17:20 LST to 19:00 LST. As time
665 progresses from 17:20 LST to 19:00 LST, overall higher condensation rates, droplet and
666 raindrop mass maintain in the control-b run (Figure 10e). Here, while the time- and
667 domain-averaged deposition (condensation and freezing) rates are lower (higher) in the
668 control-b run over the whole simulation period, the average differences in freezing rates
669 are \sim one to \sim two orders of magnitude smaller than those in deposition and condensation

670 rates between the runs. Hence, more condensation (but not deposition and freezing) is a
671 main cause of stronger updrafts in the control-b run. More condensation and more freezing
672 tend to induce increases in the mass of precipitable hydrometeors in the control-b run. Less
673 deposition tends to induce decreases in the mass of precipitable hydrometeors in the
674 control-b run. This competition between condensation, deposition and freezing leads to
675 negligible differences in the cumulative precipitation amount at the last time step between
676 the control-b and low-aerosol-b runs, although roles of freezing in this competition are
677 negligible as compared to those of condensation and deposition.

678

679 **c. Condensation frequency distributions, horizontal distributions of**
680 **condensation and precipitation, and condensation-precipitation**
681 **correlations**

682

683 Figure 11 shows the horizontal distribution of the column-averaged condensation rates over
684 the domain and Figure 12 shows the cumulative frequency distributions of column-
685 averaged condensation rates at selected times. As in the Seoul case, the horizontal
686 distribution of condensation rates is superimposed on that of precipitation rates and the
687 terrain in Figure 11. At 14:20 LST, condensation starts to occur in places with mountains,
688 which induce forced convection, and condensation is concentrated around the center of the
689 domain as marked by a yellow circle (Figures 11a and 11b). Note that condensation does
690 not occur in the plain area which is the south of the 100-m terrain-height contour line
691 (Figures 11a and 11b). Due to higher concentrations of aerosols acting as CCN, there is
692 more condensation around the center in the control-b run than in the low-aerosol-b run
693 (Figures 11a and 11b). This leads to a situation where the control-b run has the higher area-
694 averaged condensation rates than the low-aerosol-b run (Figure 10a). Then, as time
695 progresses to 17:20 LST, the condensation area extends to the eastern and western parts of
696 the domain mostly over mountain areas (Figures 11c and 11d). Hence, the main source of
697 condensation is considered to be forced convection over mountains. As seen in Figures 11c
698 and 11d, higher concentrations of aerosols acting as CCN induce the control-b run to have
699 much more condensation spots and thus much bigger areas with condensation than the low-
700 aerosol-b run at 17:20 LST. Associated with this, CCN-induced more condensation in the

701 control-b run maintains with the time progress to 17:20 LST (Figure 10d). At 17:20 LST,
702 precipitation mainly occurs in a spot which is in the western part of areas with relatively
703 high condensation rates (Figures 11c and 11d).

704 At 17:20 LST, as seen in the cumulative frequency of condensation rates, the control-
705 b run has the higher condensation frequency above condensation rate of $\sim 10 \times 10^{-3} \text{ g m}^{-3} \text{ s}^{-1}$
706 and below that of $\sim 3 \times 10^{-3} \text{ g m}^{-3} \text{ s}^{-1}$ than the low-aerosol-b run (Figure 12a). This pattern
707 of differences in the condensation frequency distribution with the tipping condensation-
708 rate points at $\sim 10 \times 10^{-3}$ and $\sim 3 \times 10^{-3} \text{ g m}^{-2} \text{ s}^{-1}$ continues up to 19:00 LST (Figures 12b).
709 Figure 13 shows the mean precipitation rate over each of the column-averaged
710 condensation rates for the period up to 17:20 LST in the control-b run. A column-averaged
711 condensation rate in an air column with a precipitation rate at its surface is obtained and
712 these condensation and precipitation rates are paired at each column and time step. Then,
713 collected precipitation rates are classified and grouped based on the corresponding paired
714 column-averaged condensation rates. The classified precipitation rates corresponding to
715 each of the column-averaged condensation rates are averaged arithmetically to construct
716 Figure 13. There are only less than 10 % differences in the mean precipitation rate for each
717 of the column-averaged condensation rates between the control-b and low-aerosol-b runs
718 (not shown). Figure 13 shows that generally a higher condensation rate is related to a higher
719 mean precipitation rate. It is also roughly shown that, according to the mean precipitation
720 rate for each condensation rate, overall, condensation rates below $\sim 3 \times 10^{-3} \text{ g m}^{-3} \text{ s}^{-1}$ and
721 above $\sim 10 \times 10^{-3} \text{ g m}^{-3} \text{ s}^{-1}$ are correlated with precipitation rates below $\sim 2 \text{ mm hr}^{-1}$ and
722 above $\sim 12 \text{ mm hr}^{-1}$, respectively, while condensation rates between ~ 3 and $\sim 10 \times 10^{-3} \text{ g m}^{-3} \text{ s}^{-1}$
723 are correlated with precipitation rates between ~ 2 and $\sim 12 \text{ mm hr}^{-1}$ (Figure 13).
724 Hence, on average, the higher frequency of condensation with rates above $\sim 10 \times 10^{-3} \text{ g m}^{-3} \text{ s}^{-1}$
725 and below $\sim 3 \times 10^{-3} \text{ g m}^{-3} \text{ s}^{-1}$ can be considered to lead to the higher frequency of
726 precipitation whose rates are higher than $\sim 12 \text{ mm hr}^{-1}$ and lower than $\sim 2 \text{ mm hr}^{-1}$ in the
727 control-b run, respectively. It can also be considered that the lower condensation frequency
728 between ~ 3 and $\sim 10 \times 10^{-3} \text{ g m}^{-3} \text{ s}^{-1}$ leads to the lower precipitation frequency between ~ 2
729 and $\sim 12 \text{ mm hr}^{-1}$ in the control-b run. It is found that this correspondence between
730 condensation and precipitation rates is valid whether analyses to construct Figure 13 are
731 repeated only for a time point at 16:30 LST or for a period between 16:30 and 17:00 LST.

732 These time point and period are related to analyses of the moist static energy as described
733 in Section e below.

734 At 17:20 LST, the larger precipitation frequency between ~ 2 and ~ 12 mm hr⁻¹ in the
735 low-aerosol-b run nearly offsets the larger precipitation frequency in the other ranges of
736 precipitation rates in the control-b run (Figure 9c). This leads to the similar average
737 precipitation rate between the runs at 17:20 LST and contributes to the similar cumulative
738 precipitation at the last time step between the runs (Figure 3b).

739

740 **d. Evaporation and gust fronts**

741

742 As time progresses from 17:00 to 19:00 LST, the precipitation system moves northward
743 (Figure 14). At the core of the precipitation system, due to evaporation and downdrafts,
744 there is the horizontal outflow forming at 17:00 LST (Figures 14a and 14b). The core is
745 represented by the field of precipitation whose rates are higher than 1 mm hr⁻¹ in Figure 14.
746 At the core, the northward outflow is magnified by the northward synoptic-scale wind,
747 while at the core, the outflow in the other directions is offset by the northward synoptic-
748 scale wind. Hence, the outflow is mainly northward from 17:00 LST onwards as marked
749 by yellow circles in Figures 14. This enables convergence or a gust front, which is produced
750 by the outflow from the core, to be mainly formed at the north of the core. Note that the
751 intensity of a gust front is proportional to that of outflow from a core of precipitation or
752 convective system (Weisman and Klemp, 1982; Houze, 1993). The strong gust front at the
753 north of the core generates strong updrafts, a significant amount of condensation and
754 precipitation. Then, a subsequent area with clouds and precipitation is formed at the north
755 of the core as time progresses, which means that the precipitation system extends or moves
756 to the north as seen in comparisons between sub-panels with different times in Figure 14.
757 This movement, which is induced by collaborative work between outflow, synoptic wind
758 and gust fronts, is typical in deep convective clouds.

759 As described above, the more droplet nucleation and greater integrated droplet surface
760 induce more condensation before 17:00 LST in the control-b run. This and lower efficiency
761 of collision and collection among droplets enable the control-b run to have a larger amount
762 of cloud liquid or droplets as a source of evaporation. This in turn enables more droplet

763 evaporation, more associated cooling and stronger downdrafts, although less rain
764 evaporation is in the control-b run particularly for the period from 17:00 LST to 19:00 LST.
765 The time- and domain-averaged droplet and rain evaporation rates are 0.72 (0.31) and 0.08
766 (0.13) $\text{g m}^{-3} \text{h}^{-1}$, respectively, while the time- and domain-averaged downdraft mass flux is
767 0.15 (0.10) $\text{kg m}^{-2} \text{s}^{-1}$ over the period from 17:00 LST to 19:00 LST in the control-b (low-
768 aerosol-b) run. More evaporation of droplets and associated stronger downdrafts with
769 higher concentrations of aerosols acting as CCN have been shown by the numerous
770 previous studies (e.g., Tao et al., 2007; Tao et al., 2012; Khain et al., 2008; Lee et al., 2018).

771 During the period between 17:00 and 19:00 LST, with the development of convergence
772 or the gust front, as mentioned above, the maximum precipitation rate increases from ~ 17
773 (17) to ~ 45 (33) mm hr^{-1} in the control-b (low-aerosol-b) run (Figure 9). This indicates
774 that the gust-front development contributes to the overall intensification of the precipitation
775 system, while it moves northward. If there were only northward synoptic-scale wind with
776 no formation of the gust front, the system would move northward with less intensification.
777 Over the period from 17:00 LST to 19:00 LST, stronger downdrafts and associated stronger
778 outflow generate a stronger gust front and more subsequent condensation in the control-b
779 run. This enhances the small initial difference, which is at 17:00 LST, in the frequency of
780 precipitation with rates above $\sim 12 \text{ mm hr}^{-1}$ between the runs substantially as time
781 progresses from 17:00 LST to 19:00 LST (Figure 9). Associated with this, with the time
782 progress, the nearly identical maximum precipitation rate between the runs at 17:00 LST
783 turns into the significantly higher maximum precipitation rate in the control-b run than in
784 the low-aerosol-b run (Figure 9). Around 19:00 LST, the system enters its dissipating stage,
785 accompanying reduction in the precipitating area and the area-averaged precipitation rate
786 (Figures 3b).

787

788 **e. Moist static energy**

789

790 Condensation, which controls droplet mass and precipitation, is controlled by updrafts and
791 updrafts are in turn controlled by instability. One of important factors that maintain
792 instability is the moist static energy. Motivated by this, to better understand differences in
793 the precipitation frequency distribution in association with those in the condensation

794 frequency distribution between the control-b and low-aerosol-b runs, we calculate the flux
 795 of the moist static energy and the flux is defined as follows:

796

$$797 \quad \vec{F}_S = S \times \rho \times \vec{V} \quad (1),$$

798

799 where \vec{F}_S represents the flux of the moist static energy, S the moist static energy, ρ the air
 800 density and \vec{V} the horizontal-wind vector. In Eq. (1), we see that the flux is in the vector
 801 form and has two components, which are its magnitude and direction. The fluxes of the
 802 moist static energy in the PBL are obtained over the domain at 16:30 LST, since in general,
 803 the moist static energy in the PBL has much stronger effects on instability and updrafts
 804 than that above the PBL. In particular, we focus on the PBL fluxes of the energy that cross
 805 the boundary over a time step at 16:30 LST between areas with the column-averaged
 806 condensation rate from $3 \times 10^{-3} \text{ g m}^{-3} \text{ s}^{-1}$ to $10 \times 10^{-3} \text{ g m}^{-3} \text{ s}^{-1}$, which are referred to as “area
 807 A”, and those with the column-averaged condensation rate above $10 \times 10^{-3} \text{ g m}^{-3} \text{ s}^{-1}$, which
 808 are referred to as “area B”. This is because we are interested in the exchange of the moist
 809 static energy between areas A and B and this exchange can be seen by looking at those
 810 fluxes which cross the boundary between those areas.

811 We are interested in the exchange of the energy, since we hypothesized that the
 812 exchange somehow alters instability in each of areas A and B in a way that there are
 813 increases (decreases) in instability, the updraft intensity, condensation and precipitation
 814 with increasing concentrations of aerosols acting as CCN in area B (A), leading to the
 815 higher (lower) frequency of condensation whose rates are higher than $10 \times 10^{-3} \text{ g m}^{-3} \text{ s}^{-1}$
 816 (between 3×10^{-3} and $10 \times 10^{-3} \text{ g m}^{-3} \text{ s}^{-1}$) and precipitation whose rates are higher than 12
 817 mm hr^{-1} (between 2 and 12 mm hr^{-1}) in the control-b run than in the low-aerosol-b run.
 818 When the PBL fluxes, which crosses the boundary over the time step at 16:30 LST, are
 819 summed at 16:30 LST, there is the net flux from area A to area B. This means that there is
 820 the net transportation of the moist static energy from areas with condensation rates between
 821 3×10^{-3} and $10 \times 10^{-3} \text{ g m}^{-3} \text{ s}^{-1}$ to those with condensation rates greater than $10 \times 10^{-3} \text{ g m}^{-3}$
 822 s^{-1} in the PBL at 16:30 LST as shown in Table 2. Table 2 shows the net summed flux of the
 823 moist static energy which crosses the boundary between areas A and B in the control-b run
 824 as well as the low-aerosol-b run. To calculate the net flux at 16:30 LST in Table 2, the

825 fluxes, which cross the boundary between areas A and B over the time step at 16:30 LST,
826 only at grid points in the PBL are summed. For the calculation, the flux from area A to area
827 B has a positive sign, while the flux from area B to area A has a negative sign. Since the
828 net flux is positive for both of the runs as shown in Table 2, there is the net flux from area
829 A to area B in the PBL. The above-described analysis for the fluxes crossing the boundary
830 between areas A and B is repeated for every time step between 16:30 and 17:00 LST and
831 based on this, the net summed flux over the period between 16:30 and 17:00 LST is
832 obtained. As shown in Table 2, the net flux for the period between 16:30 and 17:00 LST is
833 also positive as in the situation only for 16:30 LST. This means that there is the net
834 transportation of the moist static energy from area A to area B in the PBL during the period
835 between 16:30 and 17:00 LST.

836 At 16:30 LST, condensation with rates above $10 \times 10^{-3} \text{ g m}^{-3} \text{ s}^{-1}$ starts to develop and
837 this forms area B. Area B has stronger updrafts via greater condensational heating than in
838 other areas, including area A, with lower condensation rates. Stronger updrafts in area B
839 induce the convergence of air and associated moist static energy from area A to area B.
840 Since the average condensation rate and updrafts at 16:30 LST over area B are higher and
841 stronger due to increasing concentrations of aerosols acting as CCN, respectively, the air
842 convergence and the associated transportation of the moist static energy in the PBL from
843 area A to area B are stronger and more, respectively, in the control-b run than in the low-
844 aerosol-b run (Table 2). Stated differently, area B steals the moist static energy from area
845 A, and this occurs more effectively in the control-b run. This increases instability and
846 further intensifies updrafts in area B, and decreases instability and weakens updrafts in area
847 A, while these increases and decreases (intensification and weakening) of instability
848 (updrafts) are greater in the control-b run for the period from 16:30 LST to 17:00 LST.
849 This increases condensation, cloud mass and precipitation whose rates are higher than 12
850 mm hr^{-1} in area B, and decreases condensation, cloud mass and precipitation whose rates
851 are from 2 mm hr^{-1} to 12 mm hr^{-1} in area A. These increases and decreases occur more
852 effectively for the control-b run than for the low-aerosol-b run during the period. This in
853 turn leads to the lower precipitation frequency for the precipitation rates from 2 mm hr^{-1} to
854 12 mm hr^{-1} and the higher frequency for the precipitation whose rates are higher than 12
855 mm hr^{-1} at 17:00 LST in the control-b run (Figure 9b). The weakened updrafts and reduced

856 condensation turn a portion of precipitation with rates between 2 and 12 mm hr⁻¹ to
857 precipitation whose rates are below 2 mm hr⁻¹, and this takes place more efficiently in the
858 control-b run during the period between 16:30 and 17:00 LST. This eventually increases
859 the frequency of precipitation rates below 2 mm hr⁻¹ and this increase is greater for the
860 control-b run, leading to the greater precipitation frequency for the precipitation rates
861 below 2 mm hr⁻¹ in the control-b run at 17:20 LST (Figure 9c).

862

863 **5. Discussion**

864

865 **5.1 Comparison of the Seoul and Beijing cases**

866

867 In this section, we compare the Seoul case to the Beijing case. For the comparison,
868 remember that on average, a pair of the control-s and low-aerosol-s runs has the same
869 perturbation of aerosols acting as CCN as in a pair of the control-b and low-aerosol-b runs.
870 Associated with the fact that clouds in the Seoul case are less deep than those in the Beijing
871 case, overall, updrafts in the Seoul case are not as strong as those in the Beijing case. Hence,
872 unlike the situation in the Beijing case, stronger updrafts, which accompany higher
873 condensation rates, and associated convergence in the Seoul case are not strong enough to
874 steal the sufficient amount of the moist static energy from weaker updrafts which
875 accompany lower condensation rates. This makes the redistribution of the moist static
876 energy between areas with relatively higher condensation rates and those with relative
877 lower condensation rates, such as that between areas A and B for the Beijing case,
878 ineffective for the Seoul case. Due to this, the sign of CCN-induced changes in the
879 frequency of precipitation rates does not vary throughout all of the precipitation rates
880 except for the range of low precipitation rates where there are nearly no CCN-induced
881 changes in the frequency in the Seoul case as shown in Figure 4a. As seen in Figure 4a,
882 mainly due to increases in condensation and deposition, precipitation frequency increases
883 for most of precipitation rates, although the precipitation frequency does not show
884 significant changes as concentration of aerosols acting as CCN increases for relatively low
885 precipitation rates in the control-s run as compared to that in the low-aerosol-s run. This
886 means that there are no tipping precipitation rates where the sign of CCN-induced changes

887 in the frequency of precipitation rates changes in the Seoul case, contributing to the higher
888 cumulative precipitation amount in the simulation with higher concentrations of aerosols
889 acting as CCN for the Seoul case, which are different from the situation in the Beijing case.

890 In the Beijing case with deeper clouds as compared to those in the Seoul case, clouds
891 develop gust fronts via strong downdrafts and associated strong outflow. These gust fronts
892 play an important role in developing strong convection and associated high precipitation
893 rates. Unlike the situation in the Seoul case, there are strong clouds and associated updraft
894 entities that are able to steal heat and moisture (or the moist static energy) as sources of
895 instability from areas with relatively less strong clouds and updrafts with medium strength;
896 note that these strong clouds here involve stronger updrafts via greater condensational
897 heating as described in Section e above and this enables these clouds to be thicker and have
898 higher cloud mass than these less strong clouds. This further intensifies strong clouds and
899 weakens less strong clouds with medium strength. Due to this, the cumulative frequency
900 of heavy (medium) precipitation in association with strong clouds (less strong clouds with
901 medium strength) increases (decreases). Some of the weakened clouds eventually produce
902 light precipitation, which increase the cumulative frequency for light precipitation. The
903 intensification of strong clouds and the weakening of less strong clouds with medium
904 strength gets more effective with increasing concentration of aerosols acting as CCN.
905 Hence, in the Beijing case, for medium precipitation in association with less strong clouds,
906 the simulation with higher concentration of aerosols acting as CCN shows the lower
907 cumulative precipitation frequency at the last time step. However, for heavy precipitation,
908 which is associated with strong clouds, and light precipitation, the simulation with higher
909 concentrations of aerosols acting as CCN shows the higher cumulative precipitation
910 frequency at the last time step. These differential responses of precipitation to increasing
911 concentration of aerosols acting as CCN among different types of precipitation occur in the
912 circumstances of the similar cumulative precipitation amount between the simulations with
913 different concentration of aerosols acting as CCN. This similar precipitation amount is due
914 to above-mentioned competition between CCN-induced changes in condensation,
915 deposition and freezing.

916 In both of the Seoul and Beijing cases, CCN-induced changes in condensation plays an
917 important role in making differences in the precipitation amount and/or the precipitation

918 frequency distribution between the simulations with different concentration of aerosols
919 acting as CCN. It is notable that in less deep clouds in the Seoul case, in addition to
920 condensation, deposition plays a role in precipitation to induce CCN-induced increases in
921 the precipitation amount. CCN-induced increases in condensation initiate the differences
922 in cloud mass and precipitation and then CCN-induced increases in deposition follow to
923 further enhance those differences. In deep clouds in the Beijing case, condensation tends
924 to induce increases in cloud mass and precipitation, while deposition tends to induce
925 decreases in cloud mass and precipitation with increasing concentration of aerosols acting
926 as CCN. Hence, as clouds get shallower and thus ice processes become less active, the role
927 of deposition in CCN-induced changes in precipitation amount turns from CCN-induced
928 suppression of precipitation to enhancement of precipitation. Here, we find that contrary
929 to the traditional understanding, the role of variation of freezing, which is induced by the
930 varying concentration of aerosols acting as CCN but not INPs, in precipitation is negligible
931 as compared to that of condensation and deposition in both of the cases.

932

933 **6. Summary and conclusions**

934

935 This study examines impacts of aerosols, which act as CCN, on clouds and precipitation in
936 two metropolitan areas, which are the Seoul and Beijing areas, in East Asia that has
937 experienced substantial increases in aerosol concentrations over the last decades. The
938 examination is performed via simulations, which use a CSRM. These simulations are for
939 deep clouds which reach the tropopause in the Beijing case and for comparatively less deep
940 clouds which do not reach the tropopause yet grow above the level of freezing in the Seoul
941 case.

942 In both of the cases, CCN-induced changes in condensation plays a critical role in
943 CCN-induced variation of precipitation properties (e.g., the precipitation amount and the
944 precipitation frequency distribution). In the Seoul case, CCN-induced increases in
945 condensation and subsequent increases in deposition lead to CCN-induced increases in the
946 precipitation frequency over most of precipitation rates and thus in the precipitation amount.
947 However, in the Beijing case, while there are increases in condensation with increasing
948 CCN concentrations, there are decreases in deposition with increasing CCN concentrations.

949 This competition between increases in condensation and decreases in deposition leads to
950 negligible CCN-induced changes in cumulative precipitation amount in the Beijing case.
951 In both of the cases, CCN-induced changes in freezing are negligible as compared to those
952 in condensation and deposition. In the Beijing case, there is another competition for the
953 moist static energy among clouds with different updrafts and condensation. This
954 competition results in CCN-induced differential changes in the precipitation frequency
955 distributions. With clouds getting deeper from the Seoul case to the Beijing case, clouds
956 and associated updrafts, which are strong enough to steal the moist static energy from other
957 clouds and their updrafts, appear. This makes strong clouds stronger and clouds with
958 medium strength weaker. With higher CCN concentrations, strong clouds steal more
959 energy, and thus strong clouds become stronger and clouds with medium strength weaker
960 with a greater magnitude. As a result of this, there are more frequent heavy precipitation
961 (whose rates are higher than 12 mm hr^{-1}) and light precipitation (whose rates are lower than
962 2 mm hr^{-1}), and less frequent medium precipitation (with rates from 2 mm hr^{-1} to 12 mm
963 hr^{-1}) with increasing CCN concentrations in the Beijing case.

964 In both of the Seoul and Beijing cases, there are mountains and they play an important
965 role in how cloud and precipitation evolve with time and space. In both of the cases, the
966 precipitating system moves or expands over mountains which induce forced convection
967 and generate condensation. This important role of mountains and forced convection in the
968 formation and evolution of the precipitation system has not been examined much in the
969 previous studies of aerosol-cloud interactions, since many of those previous studies (e.g.,
970 Jiang et al., 2006; Khain et al., 2008; Li et al., 2011; Morrison et al., 2011) have dealt with
971 convective clouds that develop over plains and oceans. Hence, findings in this study, which
972 are related to mountain-forced convection and its interactions with aerosols, can be
973 complementary to those previous studies. Stated differently, this study can shed light on
974 our path to the understanding of aerosol-cloud interactions over more general domains not
975 only with no terrain but also with terrain.

976

977

978

979

980 **Code/Data source and availability**

981

982 Our private computer system stores the code/data which are private and used in this study.
983 Note that in particular, the stored PM data are provided by the Korea Environment
984 Cooperation in South Korea and State Key Laboratory of Severe Weather in China. Upon
985 approval from funding sources, the data will be opened to the public. Projects related to
986 this paper have not been finished, thus, the sources prevent the data from being open to the
987 public currently. However, if information on the data is needed, contact the corresponding
988 author Seoung Soo Lee (slee1247@umd.edu).

989

990 **Author contributions**

991 Essential initiative ideas are provided by SSL, KJH and KHS to start this work. Simulation
992 and observation data are analyzed by SSL, JC and GK. JU and YZ review the results and
993 contribute to their improvement. CHJ and JG perform additional simulations, which are
994 required by the review process, and their basic analyses. CHJ and SKS provide ideas to
995 handle the reviewers' comments.

996

997 **Competing interests**

998 The authors declare that they have no conflict of interest.

999

1000 **Acknowledgements**

1001 This study is supported by the National Research Foundation of Korea (NRF) grant funded
1002 by the Korea government (MSIT) (No. NRF2020R1A2C1003215) and the "Construction
1003 of Ocean Research Stations and their Application Studies" project funded by the Ministry
1004 of Oceans and Fisheries, South Korea. This study is also supported by the National
1005 Research Foundation of Korea (NRF) by FRIEND (Fine Particle Research Initiative in East
1006 Asia Considering National Differences) project through the National Research Foundation
1007 of Korea (NRF) funded by the Ministry of Science and ICT (2020M3G1A1114617), and
1008 the Korea Meteorological Administration Research and Development Program "Research
1009 on Weather Modification and Cloud Physics" under Grant (KMA2018-00224). Authors
1010 thank Danhong Dong at Chinese Academy of Sciences and Fang Wu at Beijing Normal
1011 University for their reviewing this paper.

1012 **References**

1013

1014 Brown, A., Milton, S., Cullen, M., Golding, B., Mitchell, J., and Shelly, A.: Unified
1015 modeling and prediction of weather and climate: A 25-year journey, *Bull. Am*
1016 *Meteorol. Soc.* 93, 1865–1877, 2012.

1017 Chen, F., and Dudhia, J.: Coupling an advanced land-surface hydrology model with the
1018 Penn State-NCAR MM5 modeling system. Part I: Model description and
1019 implementation, *Mon. Wea. Rev.*, 129, 569–585, 2001.

1020 Dong, B., Wilcox, L. J., Highwood, E. J., and Sutton, R. T.: Impacts of recent decadal
1021 changes in Asian aerosols on the East Asian summer monsoon: roles of aerosol–
1022 radiation and aerosol–cloud interactions, *Clim. Dyn.*, 53, 3235–3256, 2019.

1023 Eun, S.-H., Kim, B.-G., Lee, K.-M., and Park, J.-S.: Characteristics of recent severe haze
1024 events in Korea and possible inadvertent weather modification, *SOLA*, 12, 32–36,
1025 2016.

1026 Fan, J., Yuan, T., Comstock, J. M., et al.: Dominant role by vertical wind shear in regulating
1027 aerosol effects on deep convective clouds, *J. Geophys. Res.*, 114,
1028 doi:10.1029/2009JD012352, 2009.

1029 Fouquart, Y., and Bonnel, B.: Computation of solar heating of the Earth's atmosphere: a
1030 new parameterization, *Beitr. Phys. Atmos.*, 53, 35–62, 1980.

1031 Ha, K.-J., Nam, S., Jeong, J.-Y., et al., Observations utilizing Korean ocean research
1032 stations and their applications for process studies, *Bull. Amer. Meteor. Soc.*, 100,
1033 2061–2075, 2019.

1034 Holben, B. N., Tanré, D., Smirnov, et al.: An emerging ground-based aerosol climatology:
1035 Aerosol optical depth from AERONET, *J. Geophys. Res.*, 106, 12067–12097, 2001.

1036 Houze, R. A., *Cloud dynamics*, Academic Press, 573 pp, 1993.

1037 Hwang, S.-O., and Lee, D.-K.: A study on the relationship between heavy rainfalls and
1038 associated low-level jets in the Korean peninsula, *J. Korean. Meteorol. Soc.*, 29, 133–
1039 146, 1993.

1040 Jiang, H., Xue, H., Teller, A., Feingold, G., and Levin, Z.: Aerosol effects on the lifetime
1041 of shallow cumulus, *Geophys. Res. Lett.*, 33, L14806, doi:10.1029/2006GL026024,
1042 2006.

- 1043 Kar, S. K., Lioi, Y.A., and Ha, K.-J. : Aerosol effects on the enhancement of cloud-to-
1044 ground lightning over major urban areas of South Korea, *Atmos. Res.* , 92, 80-87,
1045 2009.
- 1046 Khain, A., BenMoshe, N., and Pokrovsky, A.: Factors determining the impact of aerosols
1047 on surface precipitation from clouds: Attempt of classification, *J. Atmos. Sci.*, 65,
1048 1721-1748, 2008.
- 1049 Khain, A., Pokrovsky, A., Rosenfeld, D., Blahak, U., and Ryzhkoy, A.: The role of CCN in
1050 precipitation and hail in a mid-latitude storm as seen in simulations using a spectral
1051 (bin) microphysics model in a 2D dynamic frame, *Atmos. Res.*, 99, 129–146, 2011.
- 1052 Khain, A., Rosenfeld, D., and Pokrovsky, A.: Aerosol impact on the dynamics and
1053 microphysics of deep convective clouds, *Quart. J. Roy. Meteor. Soc.*, 131, 2639-266,
1054 2005.
- 1055 Khain, A. D., BenMoshe, N., and A. Pokrovsky, A.: Factors determining the impact of
1056 aerosols on surface precipitation from clouds: An attempt at classification, *J. Atmos.*
1057 *Sci.*, 65, 1721–1748, doi:10.1175/2007JAS2515.1, 2008.
- 1058 King, J.: Automatic weather stations, available at
1059 [https://web.archive.org/web/20090522121225/http://www.automaticweatherstation.c](https://web.archive.org/web/20090522121225/http://www.automaticweatherstation.com/index.html)
1060 [om/index.html](https://web.archive.org/web/20090522121225/http://www.automaticweatherstation.com/index.html), 2009.
- 1061 Koop, T., Luo, B. P., Tsias, A., and Peter, T.: Water activity as the determinant for
1062 homogeneous ice nucleation in aqueous solutions, *Nature*, 406, 611-614, 2000.
- 1063 Lebo, Z. J., and Morrison, H.: Dynamical effects of aerosol perturbations on simulated
1064 idealized squall lines, *Mon. Wea. Rev.*, 142, 991-1009, 2014.
- 1065 Lee, D.-K., Kim, H.-R., and Hong, S.-Y.: Heavy rainfall over Korea during 1980–1990.
1066 Korean, *J. Atmos. Sci.*, 1, 32–50, 1998.
- 1067 Lee, S., Ho, C.-H., Lee, Y. G., Choi, H.-J. and Song, C.-K.: Influence of transboundary air
1068 pollutants from China on the high-PM10 episode in Seoul, Korea for the period
1069 October 16–20, 2008. *Atmos. Environ.*, 77, 430–439, 2013.
- 1070 Lee, S. S., Donner, L. J., Phillips, V. T. J., and Ming, Y.: The dependence of aerosol effects
1071 on clouds and precipitation on cloud-system organization, shear and stability, *J.*
1072 *Geophys. Res.*, 113, D16202, 2008.
- 1073 Lee, S. S., Kim, B.-G., and Yum, S. S., et al.: Effect of aerosol on evaporation, freezing and

- 1074 precipitation in a multiple cloud system, *Clim. Dyn.*, 48, 1069-1087, 2016.
- 1075 Lee, S. S., Li, Z., Mok, J., et al.: Interactions between aerosol absorption, thermodynamics,
1076 dynamics, and microphysics and their impacts on clouds and precipitation in a
1077 multiple-cloud system, *Clim. Dyn.*, <https://doi.org/10.1007/s00382-017-3552-x>,
1078 2017.
- 1079 Lee, S. S., Kim, B.-G., Li, Z., Choi, Y.-S., Jung, C.-H., Um, J., Mok, J., and Seo, K.-H.:
1080 Aerosol as a potential factor to control the increasing torrential rain events in urban
1081 areas over the last decades, *Atmos. Chem. Phys.*, 18, 12531–12550,
1082 <https://doi.org/10.5194/acp-18-12531-2018>, 2018.
- 1083 Li, Z., Niu, F., Fan, J., Liu, Y., Rosenfeld, D., and Ding, Y.: Long-term impacts of aerosols
1084 on the vertical development of clouds and precipitation, *Nat. Geosci.*, 4, 888-894,
1085 2011.
- 1086 Lohmann, U. and Diehl, K.: Sensitivity studies of the importance of dust ice nuclei for the
1087 indirect aerosol effect on stratiform mixed-phase clouds, *J. Atmos. Sci.*, 63, 968-982,
1088 2006.
- 1089 Lu, Z., Zhang, Q., and Streets, D. G.: Sulfur dioxide and primary carbonaceous aerosol
1090 emissions in China and India, 1996–2010, *Atmos. Chem. Phys.*, 11, 9839–9864, 2011.
- 1091 Mlawer, E. J., Taubman, S. J., Brown, P. D., Iacono, M. J., and Clough, S. A.: RRTM, a
1092 validated correlated-k model for the longwave, *J. Geophys. Res.*, 102, 16663-16668,
1093 1997.
- 1094 Möhler, O., et al, Efficiency of the deposition mode ice nucleation on mineral dust particles,
1095 *Atmos. Chem. Phys.*, 6, 3007-3021, 2006.
- 1096 Morrison, H., and Grabowski, W. W.: Cloud-system resolving model simulations of aerosol
1097 indirect effects on tropical deep convection and its thermodynamic environment,
1098 *Atmos. Chem. Phys.*, 11, 10503–10523, 2011.
- 1099 Oh, H., Ha, K.-J. and Timmermann, A.: Disentangling Impacts of Dynamic and
1100 Thermodynamic Components on Late Summer Rainfall Anomalies in East Asia, *J.*
1101 *Geophys. Res.*, 123, 8623-8633, 2018.
- 1102 Oh, H.-R., Ho, C.-H., Kim, J., Chen, D., Lee, S., Choi, Y.-S., Chang, L.-S., and Song, C.-
1103 K.: Long-range transport of air pollutants originating in China: A possible major cause
1104 of multi-day high-PM10 episodes during cold season in Seoul, Korea. *Atmos.*

- 1105 Environ., 109, 23–30, 2015.
- 1106 Pruppacher, H. R. and Klett, J. D.: Microphysics of clouds and precipitation, 714pp, D.
1107 Reidel, 1978.
- 1108 Rosenfeld, D., Lohmann, U., Raga, G. B., et al.: Flood or drought, How do aerosols affect
1109 precipitation? *Science*, 321, 1309-1313, 2008.
- 1110 Storer, R. L., van den Heever, S. C., and Stephens, G. L.: Modeling aerosol impacts on
1111 convection under differing storm environments, *J. Atmos. Sci.*, 67, 3904-3915, 2010.
- 1112 Seo, K.-H., Son, J. H., Lee, J.-H., and Park, H.-S.: Northern East Asian monsoon
1113 precipitation revealed by air mass variability and its prediction, *J. Clim.*, 28, 6221-
1114 6233, 2013.
- 1115 Tao, W.-K., Chen, J.-P., Li, Z., Wang, C., and Zhang, C.: Impact of aerosols on convective
1116 clouds and precipitation, *Rev. Geophys.*, 50, RG2001, 2012.
- 1117 Tao, W. K., Cloud resolving modeling, *J. Meteorol. Soc. Jpn.*, 85B, 305–330,
1118 doi:10.2151/jmsj.85B.305, 2007.
- 1119 van den Heever, S. C., Carrió, G. G., Cotton, W. R., DeMott, P. J., and Prenni, A. J.:
1120 Impacts of nucleating aerosol on Florida storms. part I: Mesoscale simulations, *J.*
1121 *Atmos. Sci.*, 63, 1752–1775, 2006.
- 1122 Wang, H., Skamarock, W. C., and Feingold, G.: Evaluation of scalar advection schemes in
1123 the Advanced Research WRF model using large-eddy simulations of aerosol-cloud
1124 interactions, *Mon. Wea. Rev.*, 137, 2547-2558, 2009.
- 1125 Weisman, M. L., and Klemp, J. B.: The dependence of numerically simulated convective
1126 storms on vertical wind shear and buoyancy, *Mon. Wea. Rev.*, 110, 504-520, 1982.
- 1127
- 1128
- 1129
- 1130
- 1131
- 1132
- 1133
- 1134
- 1135
- 1136
- 1137
- 1138
- 1139

1140 **FIGURE CAPTIONS**

1141

1142 Figure 1. Inner rectangles in (a) and (b) mark the Seoul area in the Korean Peninsula and
1143 the Beijing area in the East-Asia continent, respectively. A dot outside the inner rectangle
1144 in (a) marks Baekryongdo island. Dots in the inner rectangles in (a) and (b) mark the
1145 selected locations where precipitation and aerosol mass are measured. In (a) and (b), the
1146 light blue represents the ocean and the green the land area.

1147

1148 Figure 2. Time series of $PM_{2.5}$ observed at the ground station in Baekryongdo island (blue
1149 line) and of the average $PM_{2.5}$ over ground stations in the Seoul area (red line) between
1150 07:00 LST on December 22nd and 21:00 LST on December 24th in 2017. Note that $PM_{2.5}$
1151 observed at stations in the Seoul area is applied to the control-s run whose period is marked
1152 by the dashed rectangle. Time series of the average $PM_{2.5}$ over stations in the Seoul area in
1153 the low-aerosol-s run for the simulation period is also shown (black solid line).

1154

1155 Figure 3. Time series of precipitation rates at the surface, which are averaged over the
1156 domain and smoothed over 1 hour, (a) for the control-s and low-aerosol-s runs in the Seoul
1157 area and (b) for the control-b and low-aerosol-b runs in the Beijing area. In (a) and (b), the
1158 averaged and observed precipitation rates over the observation sites in the Seoul and
1159 Beijing areas, respectively, are also shown.

1160

1161 Figure 4. Observed and simulated cumulative frequency distributions of precipitation rates
1162 at the surface for (a) the Seoul case, which are collected over the Seoul area, and (b) the
1163 Beijing case, which are collected over the Beijing area, at the last time step. Simulated
1164 distributions are in the control-s and low-aerosol-s runs for the Seoul case and in the
1165 control-b and low-aerosol-b runs for the Beijing case. The observed distribution is obtained
1166 by interpolating and extrapolating the observed precipitation rates to grid points and time
1167 steps in the control-s and control-b runs for the Seoul and Beijing cases, respectively.

1168

1169 Figure 5. Cumulative frequency distributions of the precipitation rates at the surface in the
1170 control-s and low-aerosol-s runs for the Seoul case at (a) 06:00, (b) 10:00 and (c) 12:00
1171 LST.

1172

1173 Figure 6. Vertical distributions of differences in the area-averaged condensation,
1174 deposition and freezing rates, and cloud-liquid, raindrop, snow and hail mass density, and
1175 updraft mass fluxes between the control-s and low-aerosol-s runs at (a) 03:20, (b) 03:40,
1176 (c) 06:00 and (d) 12:00 LST. The horizontal black line in each panel represents the altitude
1177 of freezing or melting. Here, for the sake of the display brevity, snow mass density includes
1178 ice-mass density, while hail mass density includes graupel mass density.

1179

1180 Figure 7. Spatial distributions of terrain heights, column-averaged condensation rates,
1181 surface wind vectors and precipitation rates at (a) and (b) 03:40, (c) and (d) 08:40, (e) and
1182 (f) 10:00, and (g) and (h) 12:00 LST. The distributions in the control-s run are shown in (a),
1183 (c), (e) and (g), and the distributions in the low-aerosol-s run are shown in (b), (d), (f) and
1184 (h). Condensation rates are shaded. Dark-yellow and dark-red contours represent
1185 precipitation rates at 0.5 and 3.0 mm hr⁻¹, respectively, while beige, light brown and brown
1186 contours represent terrain heights at 100, 300 and 600 m, respectively. See text for yellow
1187 rectangles in (a), (b), (e) and (f).

1188

1189 Figure 8. Cumulative frequency distributions of the column-averaged condensation rates
1190 in the control-s and low-aerosol-s runs for the Seoul case at (a) 07:20 and (b) 09:00 LST.

1191

1192 Figure 9. Cumulative frequency distributions of the precipitation rates at the surface in the
1193 control-b and low-aerosol-b runs for the Beijing case at (a) 16:00, (b) 17:00, (c) 17:20, and
1194 (d) 19:00 LST.

1195

1196 Figure 10. Same as Figure 6 but for differences between the control-b and low-aerosol-b
1197 runs at (a) 14:20, (b) 15:40, (c) 16:00, (d) 17:20 and (e) 19:00 LST.

1198

1199 Figure 11. Spatial distributions of terrain heights, column-averaged condensation rates,
1200 surface wind vectors and precipitation rates at (a) and (b) 14:20, and (c) and (d) 17:20 LST.
1201 (a) and (c) are for the control-b run and (b) and (d) are for the low-aerosol-b run.
1202 Condensation rates are shaded. Dark-yellow and dark-red contours represent precipitation
1203 rates at 1.0 and 2.0 mm hr⁻¹, respectively, while beige, light brown, brown and dark brown
1204 contours represent terrain heights at 100, 500, 1000 and 1500 m, respectively. See text for
1205 yellow circles in (a) and (b).

1206

1207 Figure 12. Cumulative frequency distributions of the column-averaged condensation rates
1208 in the control-b and low-aerosol-b runs for the Beijing case at (a) 17:20 and (b) 19:00 LST.

1209

1210 Figure 13. Mean precipitation rates corresponding to each column-averaged condensation
1211 rate for the period between 14:00 and 17:20 LST in the control-b run. One standard
1212 deviation of precipitation rates is represented by a vertical bar at each condensation rate.

1213

1214 Figure 14. Spatial distributions of precipitation rates (shaded) and wind vectors (arrows)
1215 for the Beijing case at (a) and (b) 17:00, and (c) and (d) 19:00. The distributions in the
1216 control-b run are in (a) and (c). The distributions in the low-aerosol-b run are in (b) and (d).

1217

1218

1219

1220

1221

1222

1223

1224

1225

1226

1227

1228

Simulations	Site	Concentrations of background aerosols acting as CCN
Control-s run	Seoul area	Observed and affected by the aerosol advection
Low-aerosol-s run	Seoul area	Same as those in the control-s run but unaffected by the aerosol advection
Control-b run	Beijing area	Observed
Low-aerosol-b run	Beijing area	Reduced by a factor of 3.1 as compared to those observed

1229

1230 Table 1. Summary of simulations

1231

1232

Simulations	The net flux of the moist static energy which crosses the boundary between areas A and B ($\text{J m}^{-2} \text{ s}^{-1}$)	
	At 16:30 LST	16:30 to 17:00 LST
Control-b run	1.57×10^{12}	1.07×10^{15}
Low-aerosol-b run	1.15×10^{12}	7.55×10^{14}

1233

1234 Table 2. The net flux of the moist static energy which crosses the boundary between areas

1235 A and B at 16:30 LST and for a period from 16:30 to 17:00 LST.

1236

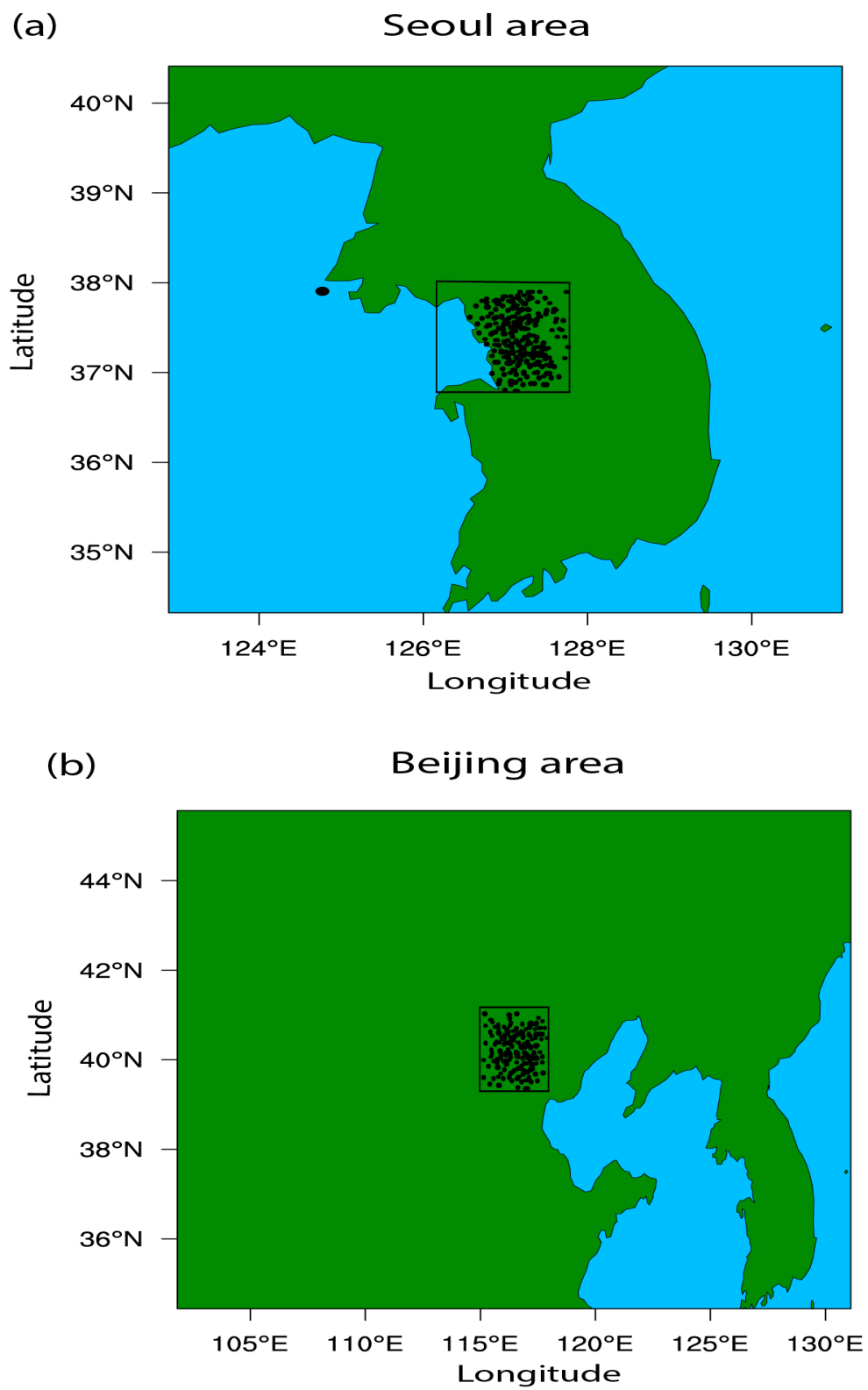
1237

1238

1239

1240

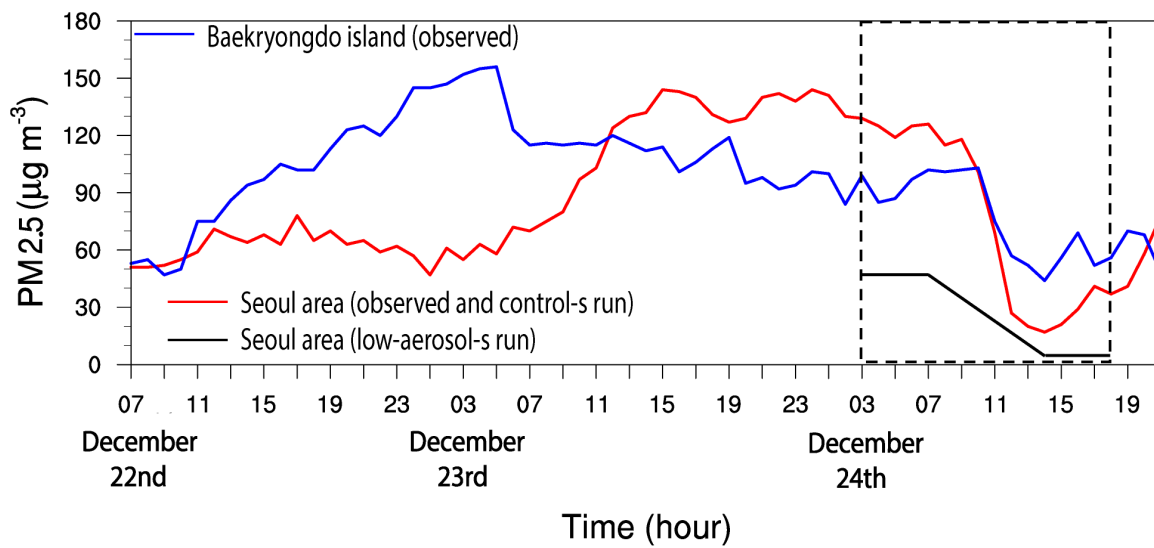
1241



1242

1243

Figure 1



1244

1245

Figure 2

1246

1247

1248

1249

1250

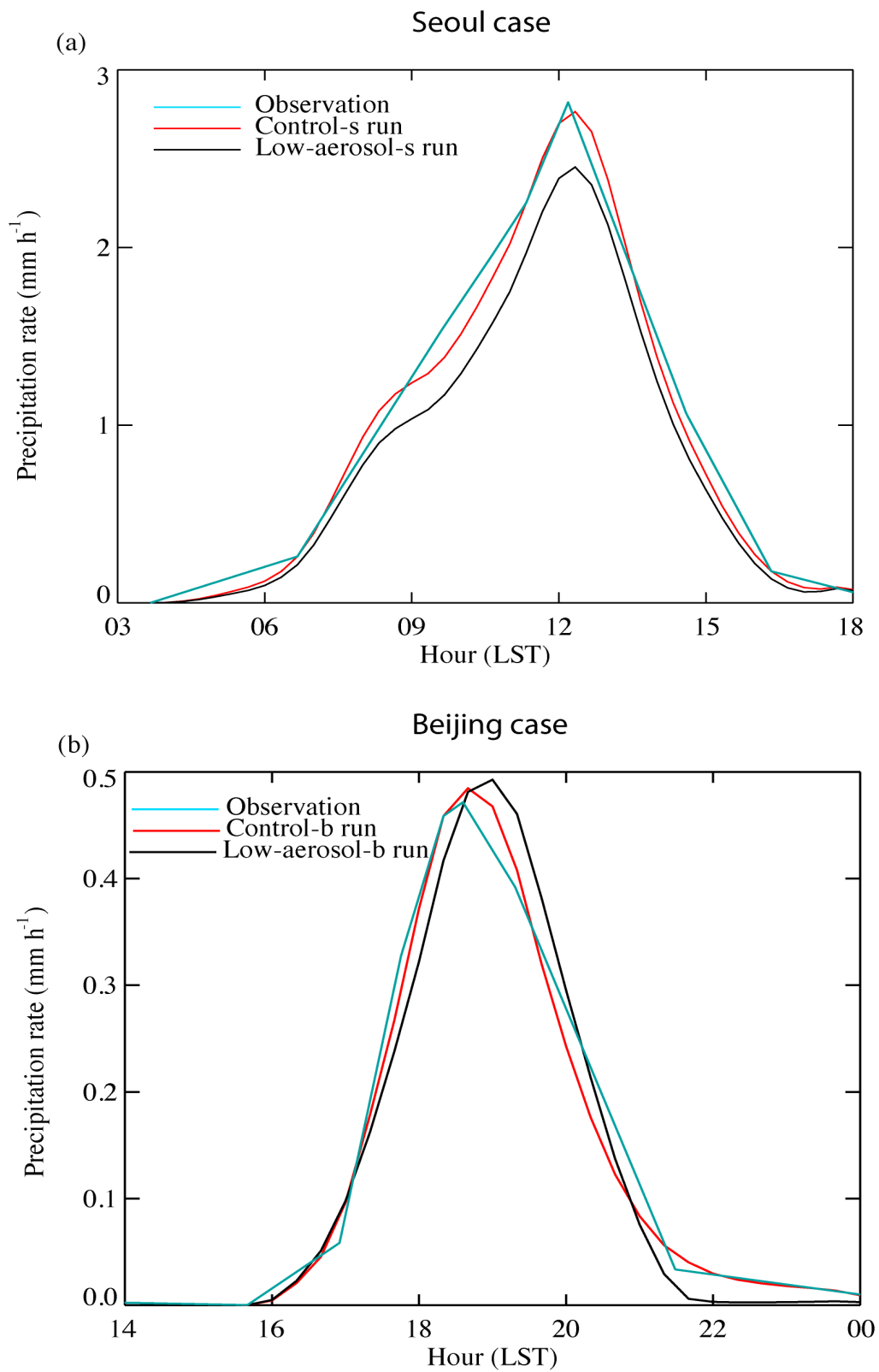
1251

1252

1253

1254

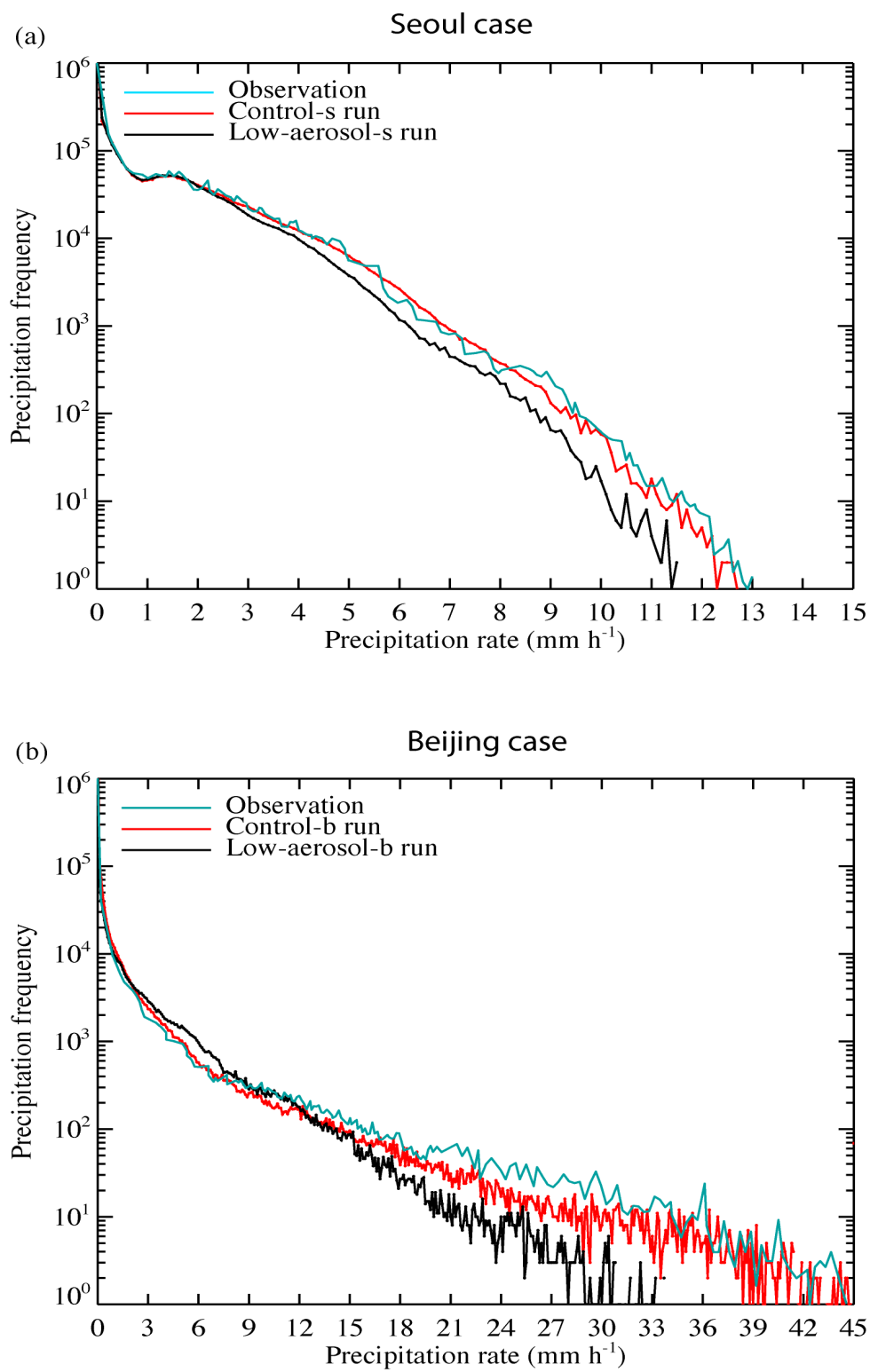
1255



1256

1257

Figure 3

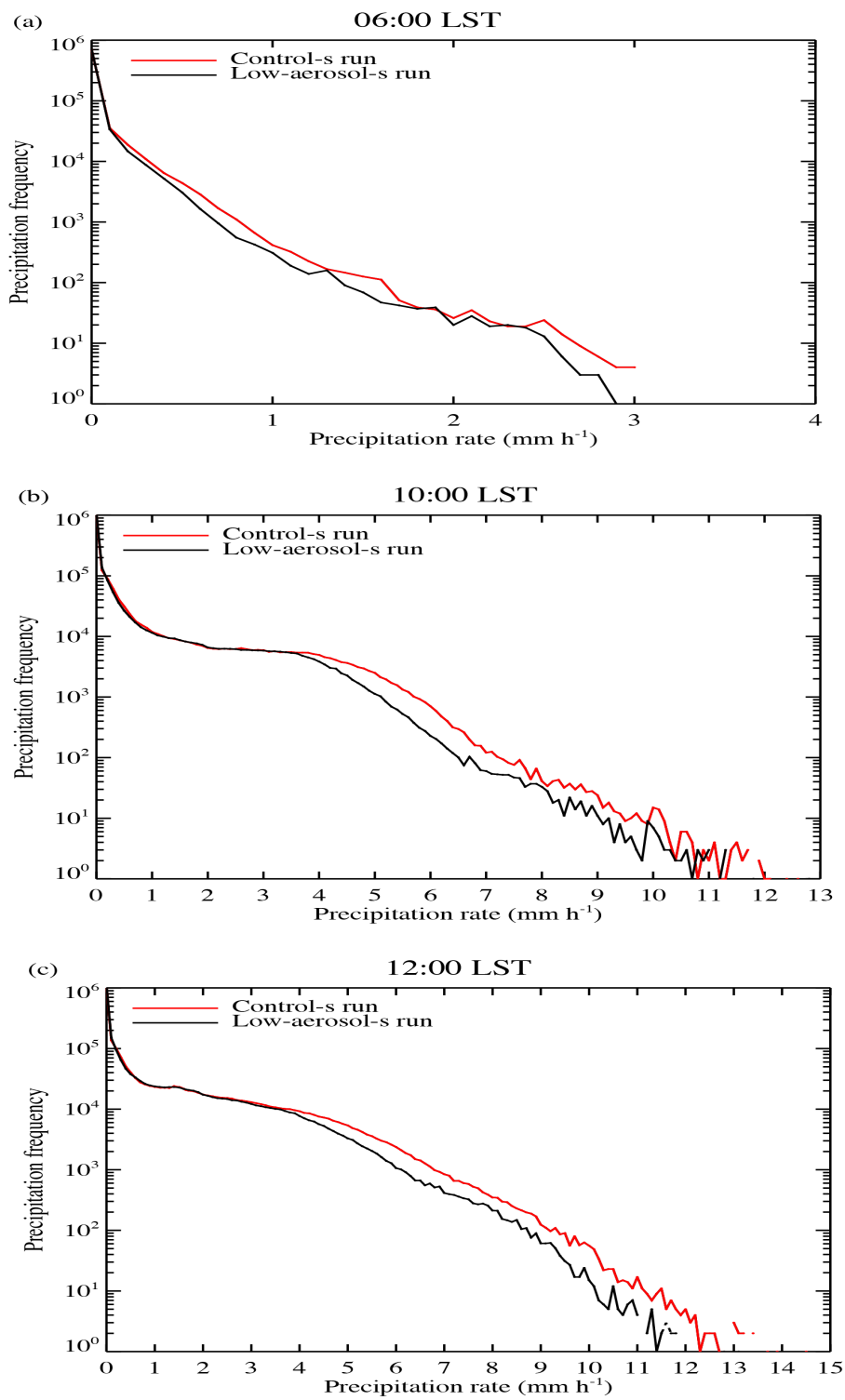


1258

1259

Figure 4

Seoul case

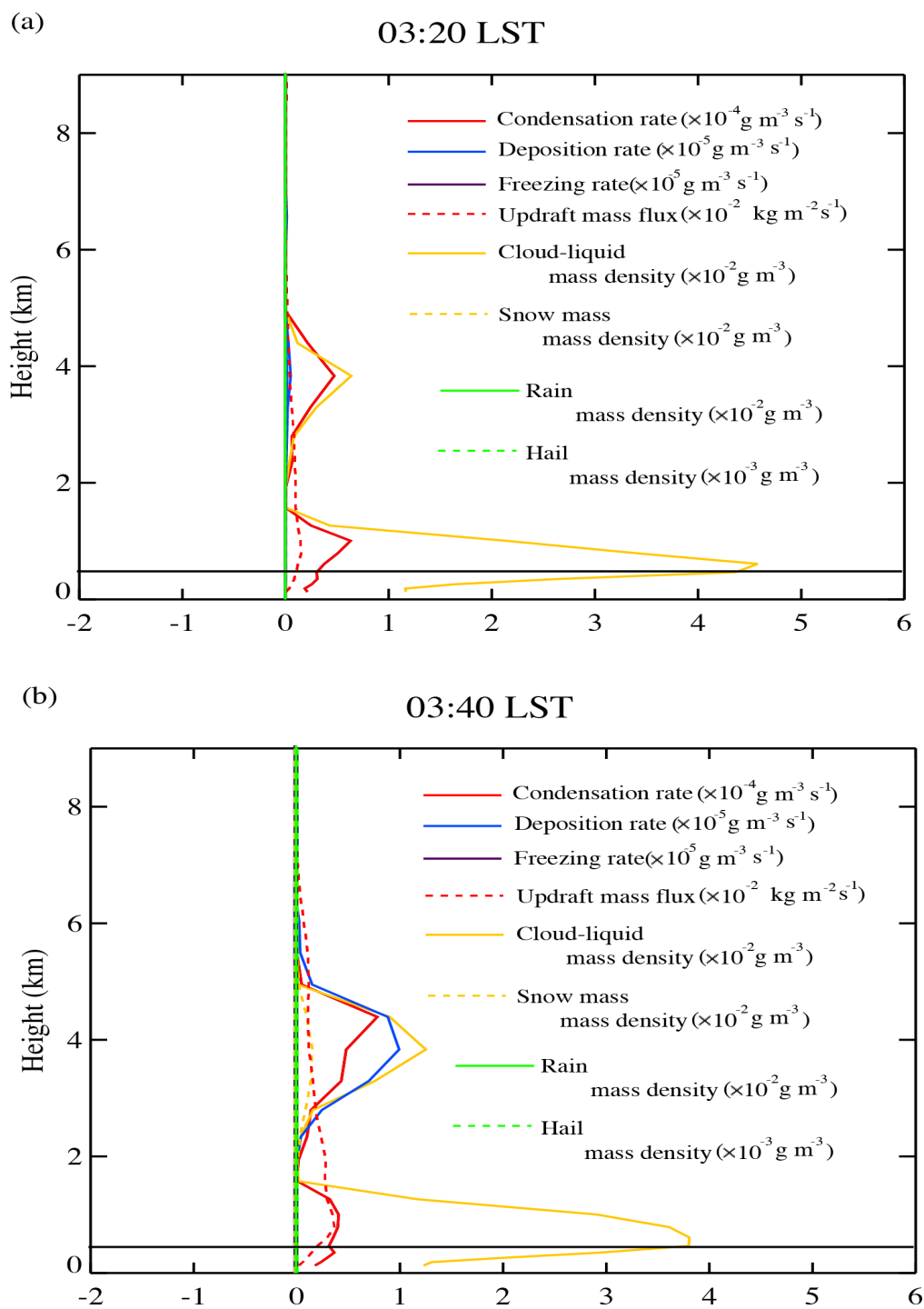


1260

1261

Figure 5

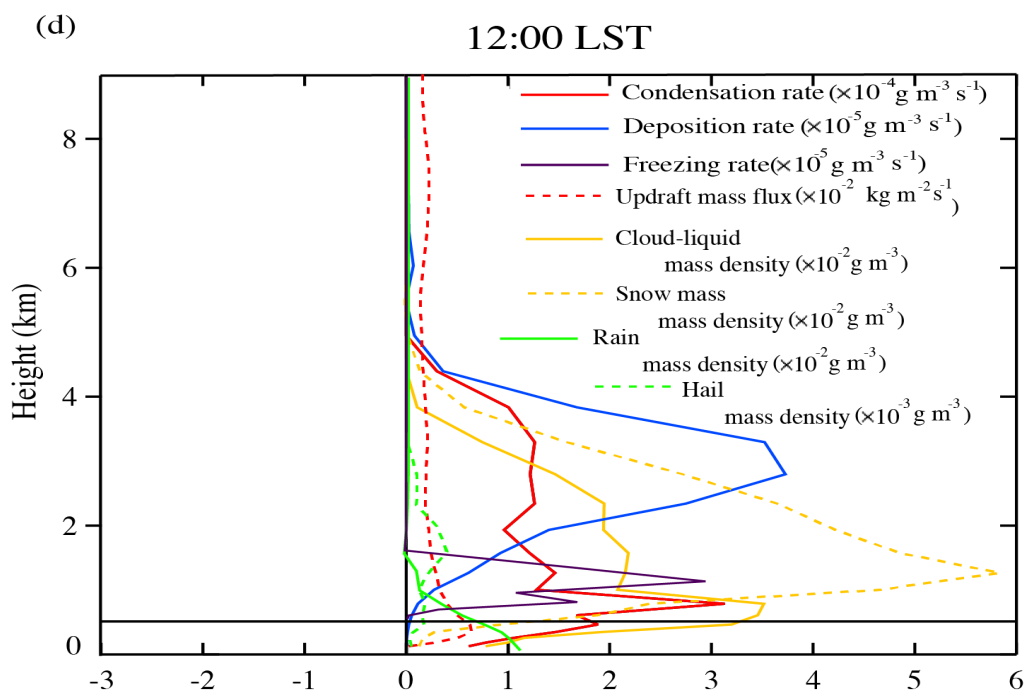
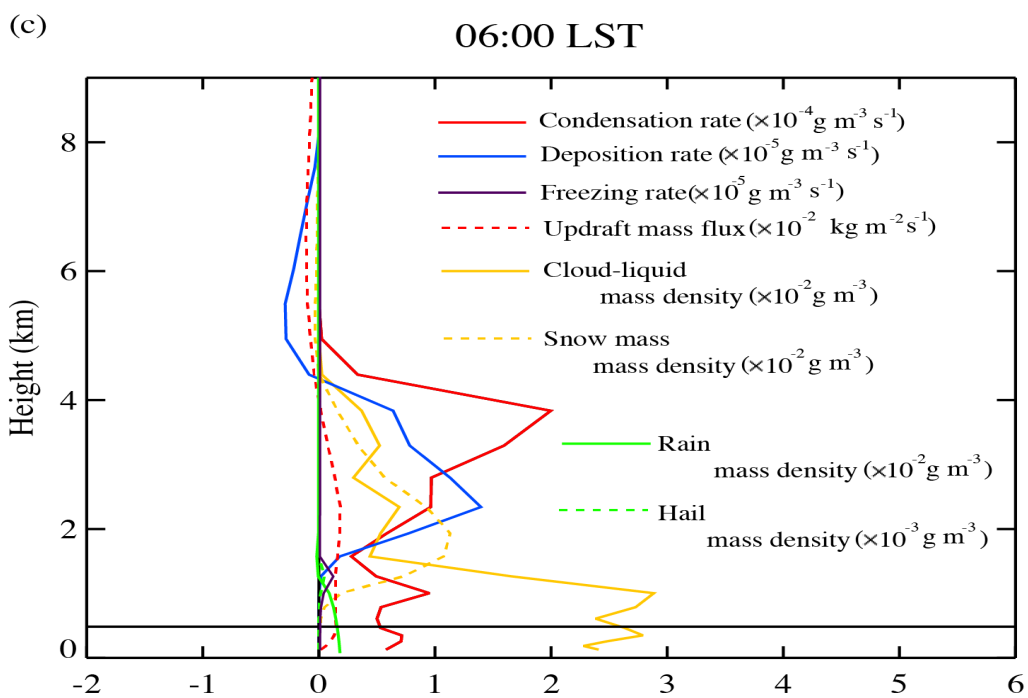
Seoul case (control-s run minus low-aerosol-s run)



1262

1263

Figure 6

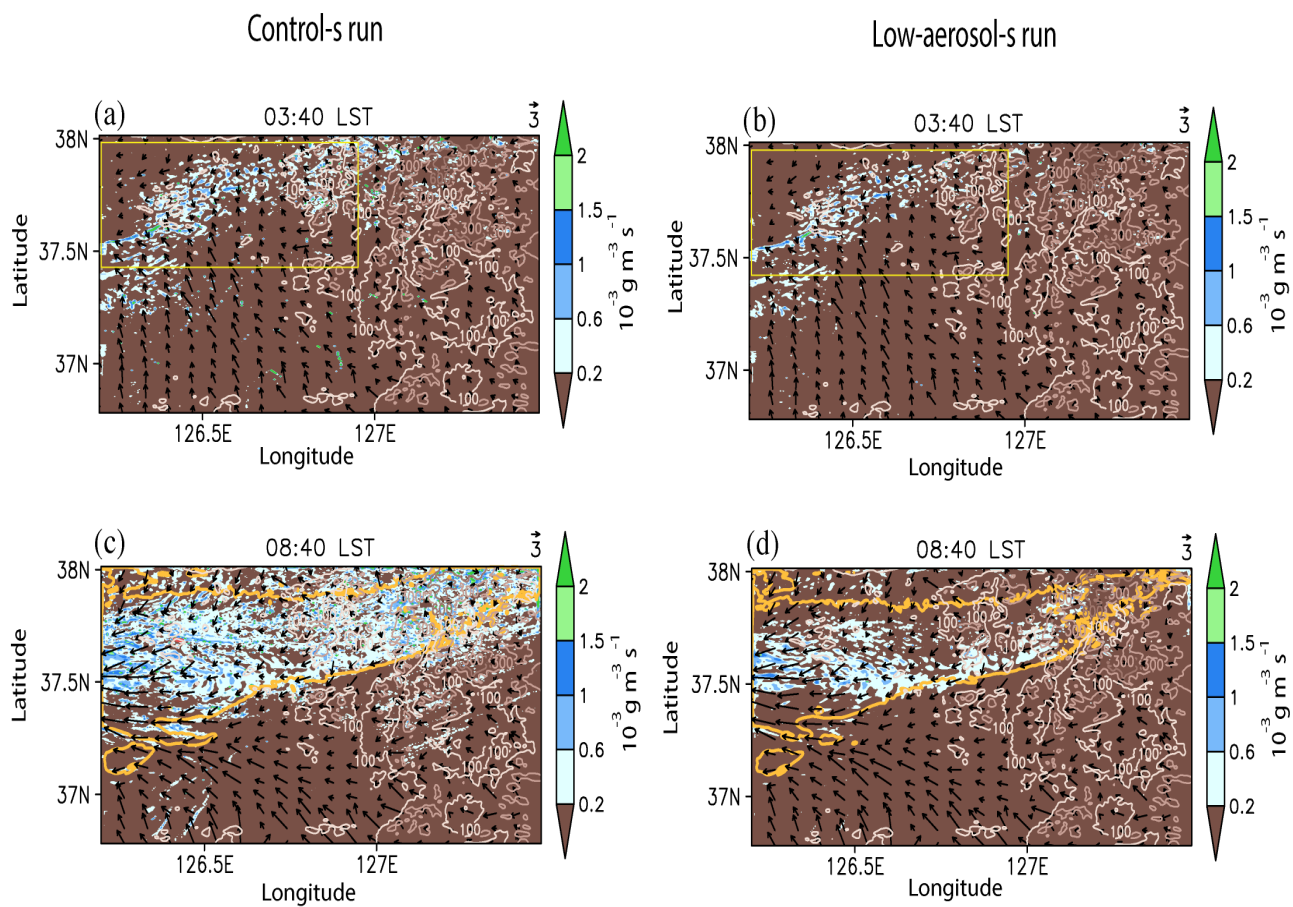


1264

1265

1266

Figure 6



1267

1268

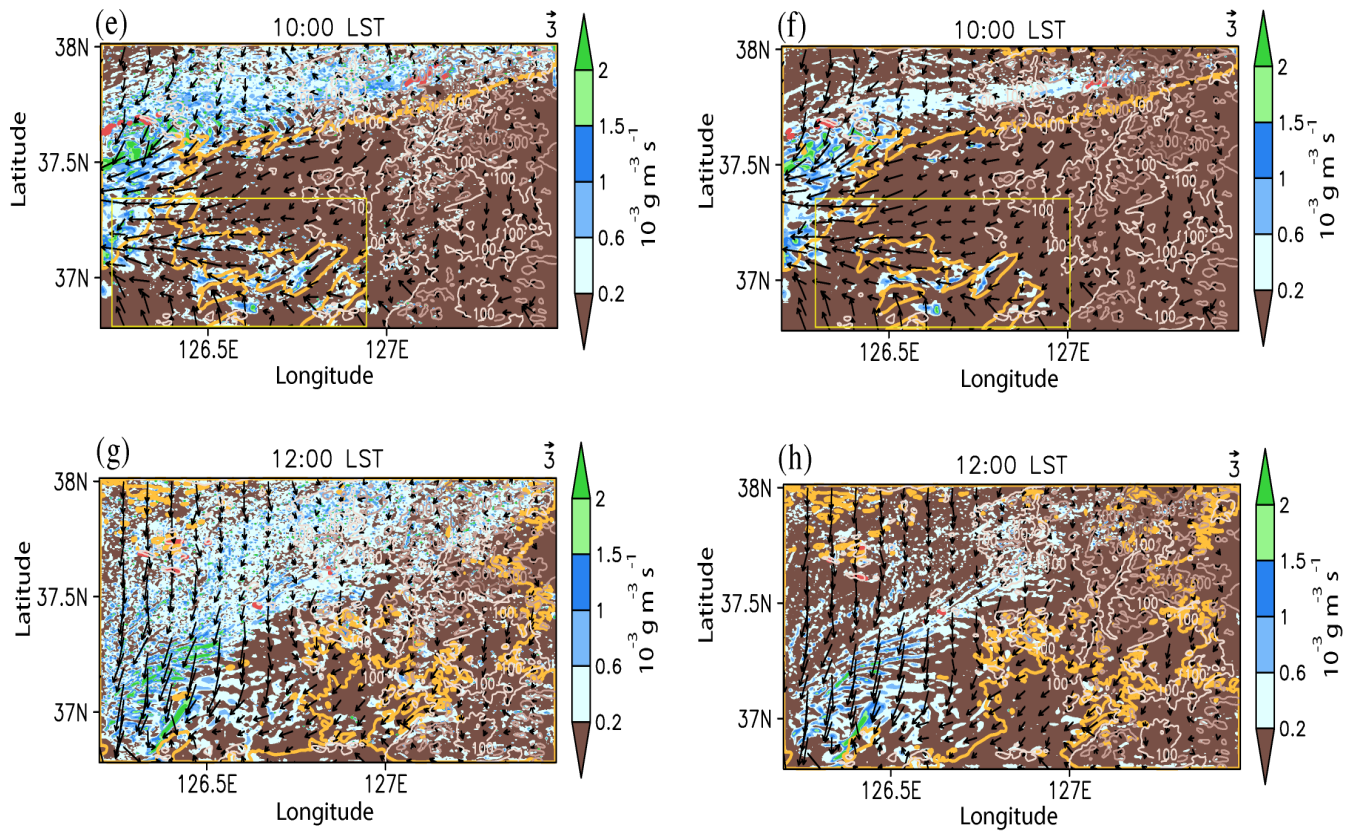
1269

1270

Figure 7

Control-s run

Low-aerosol-s run



1271

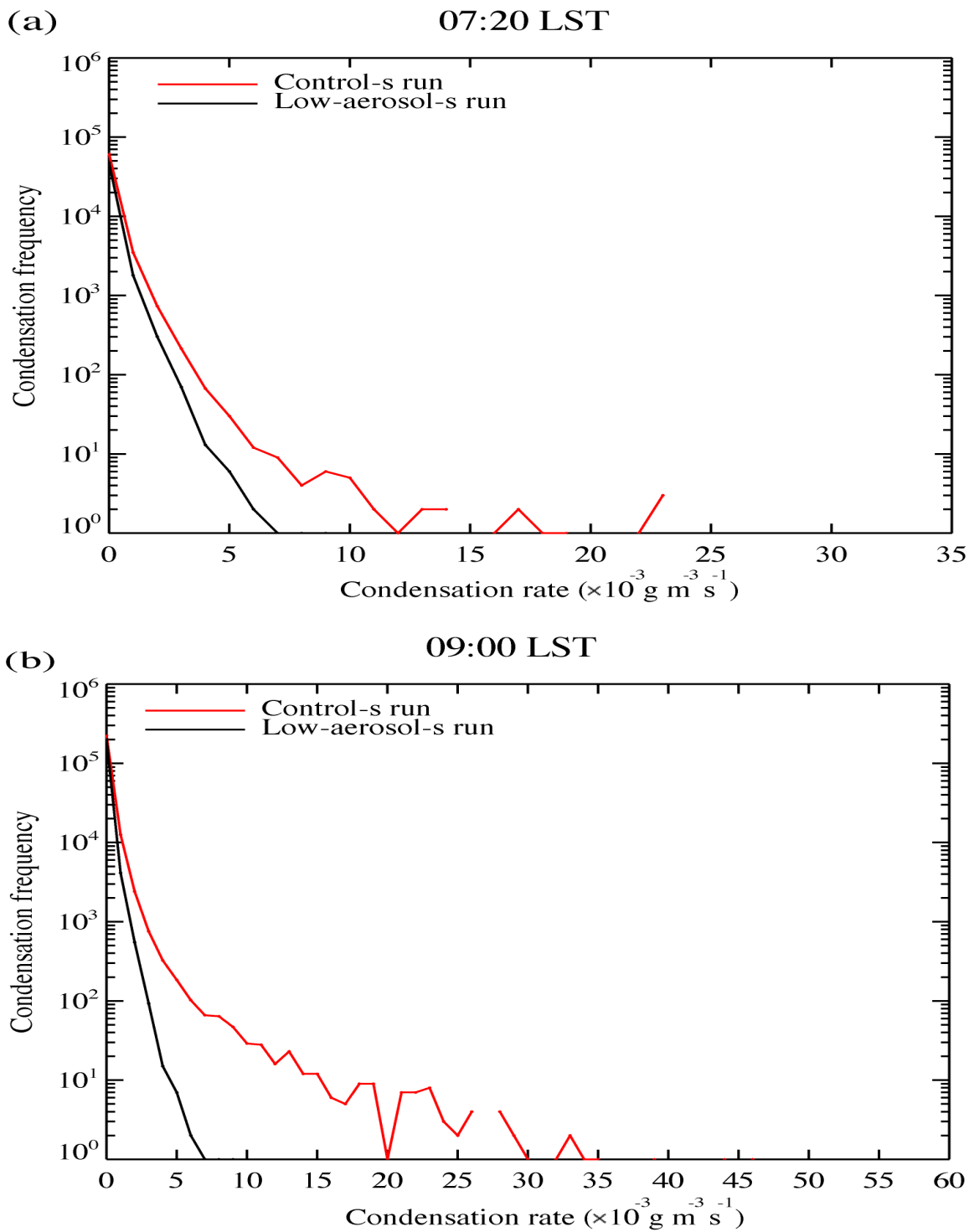
1272

1273

1274

Figure 7

Seoul case



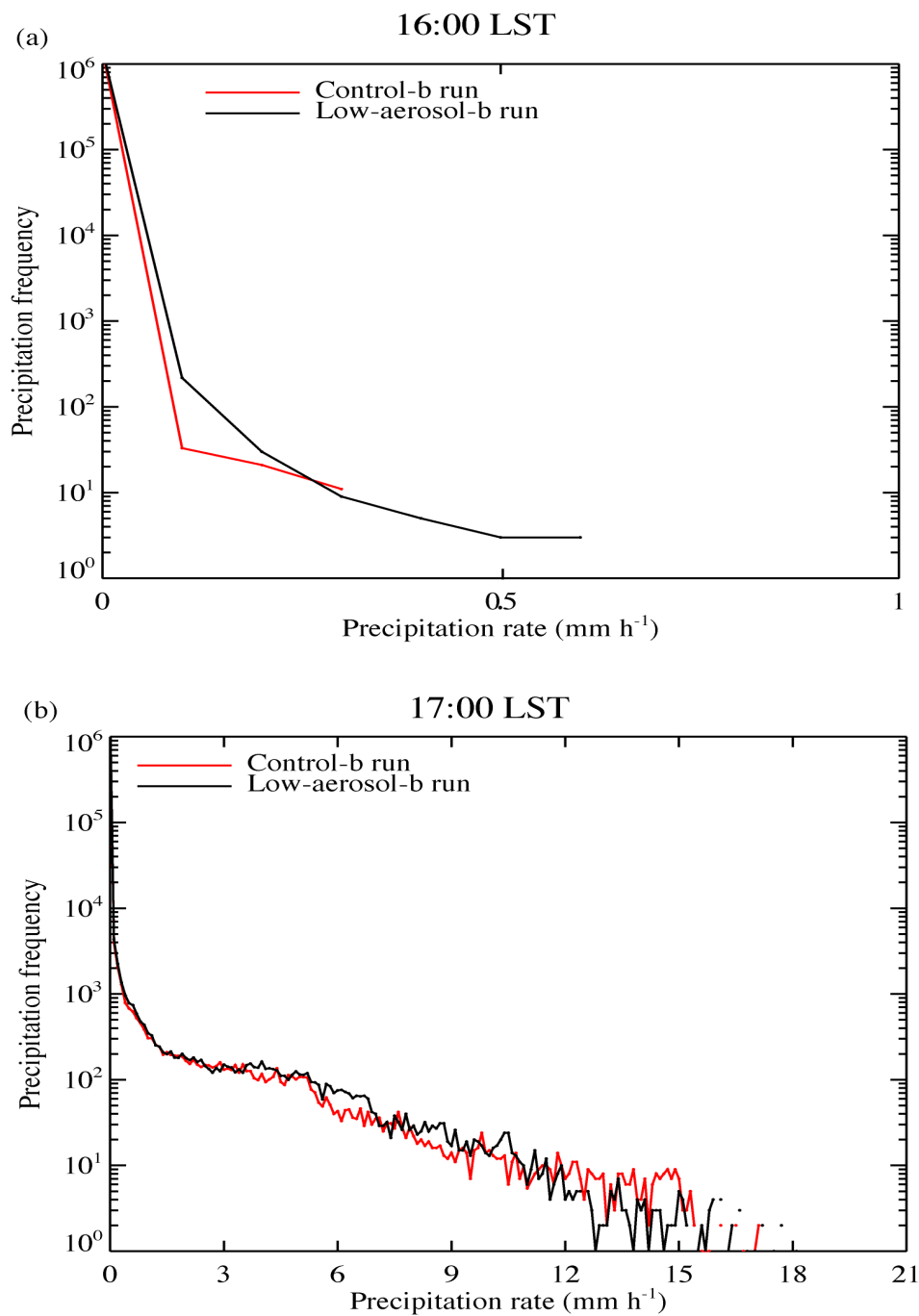
1275

1276

1277

Figure 8

Beijing case

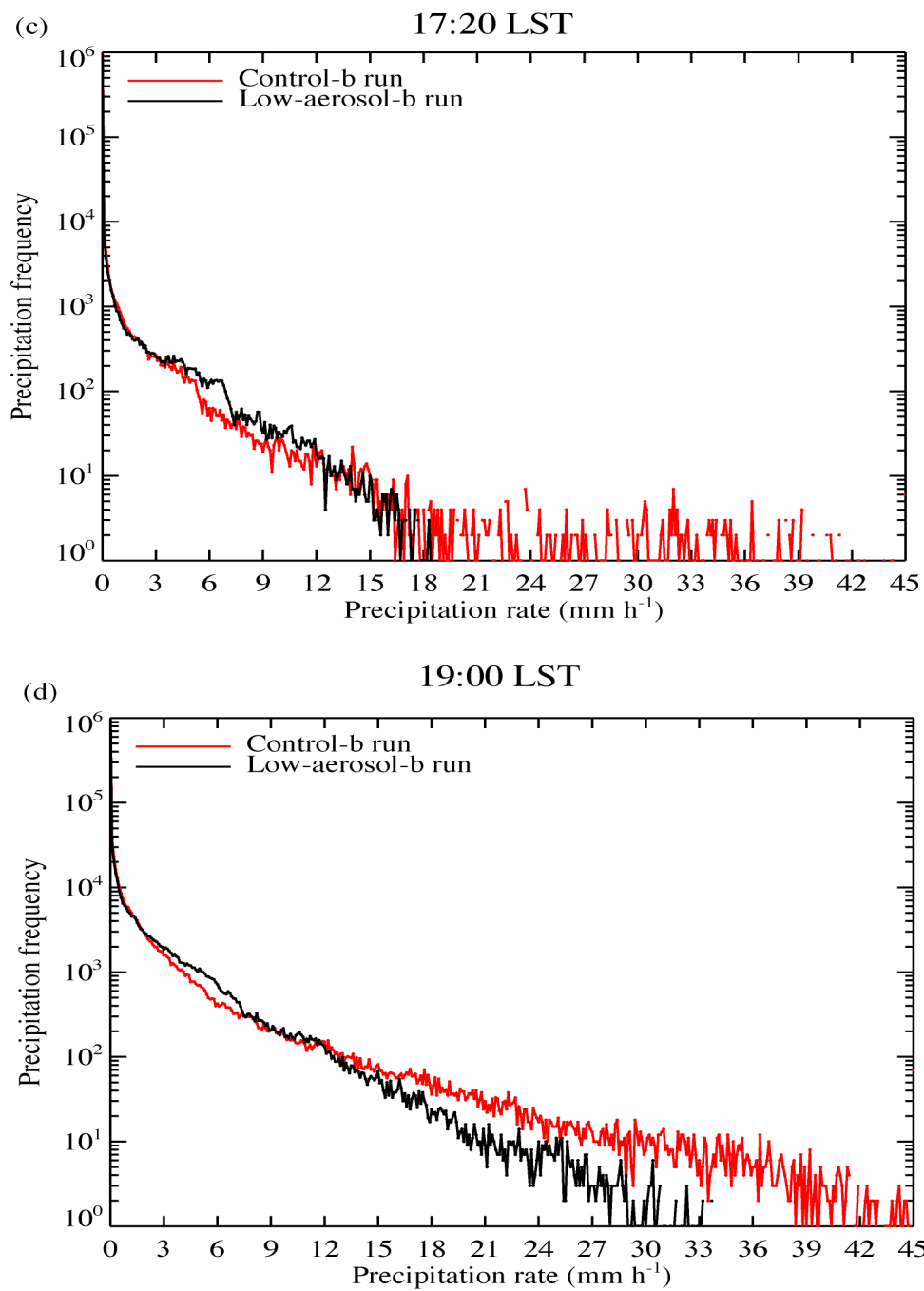


1278

1279

1280

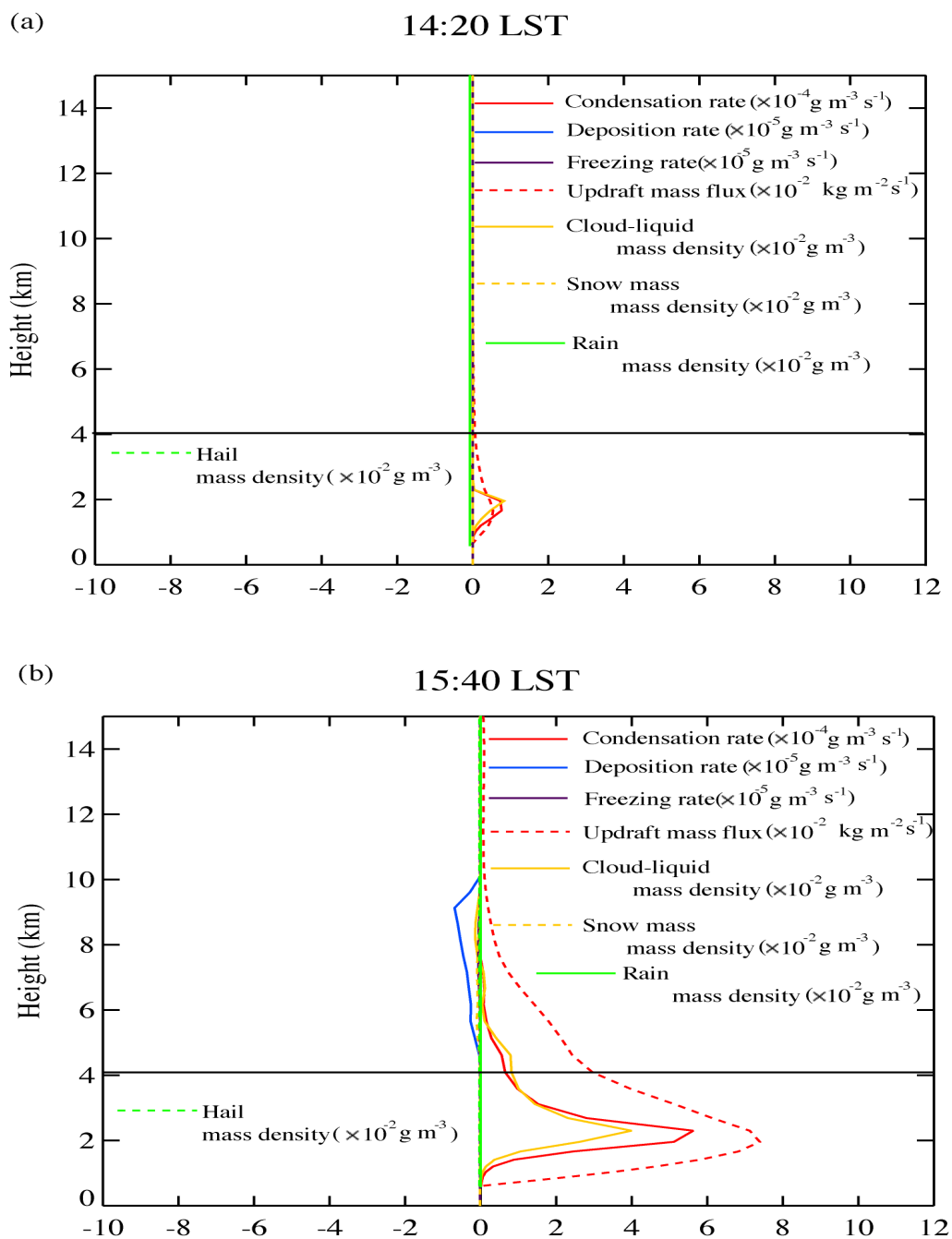
Figure 9



1281
1282
1283
1284
1285
1286

Figure 9

Beijing case (control-b run minus low-aerosol-b run)



1287

1288

Figure 10

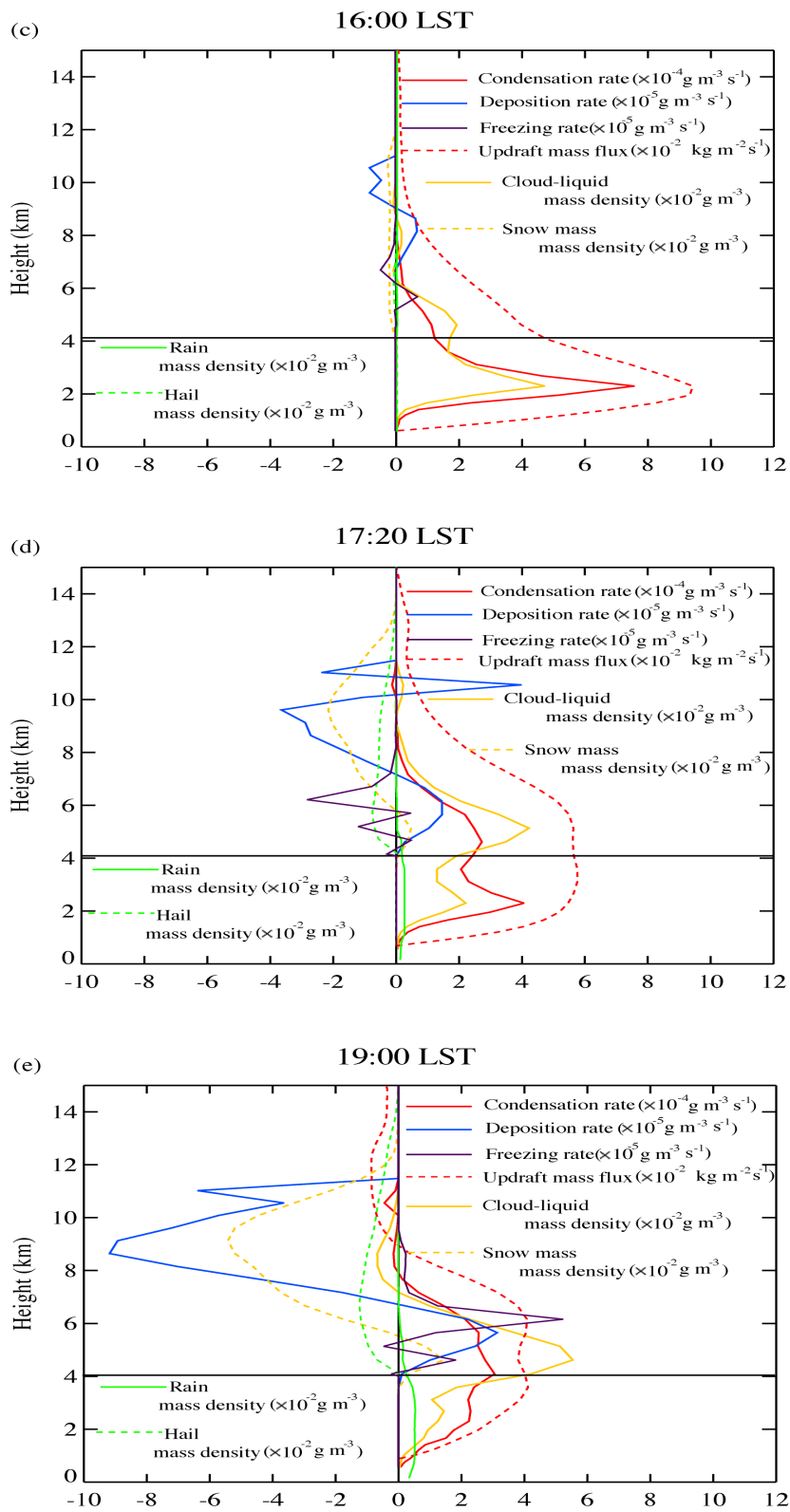
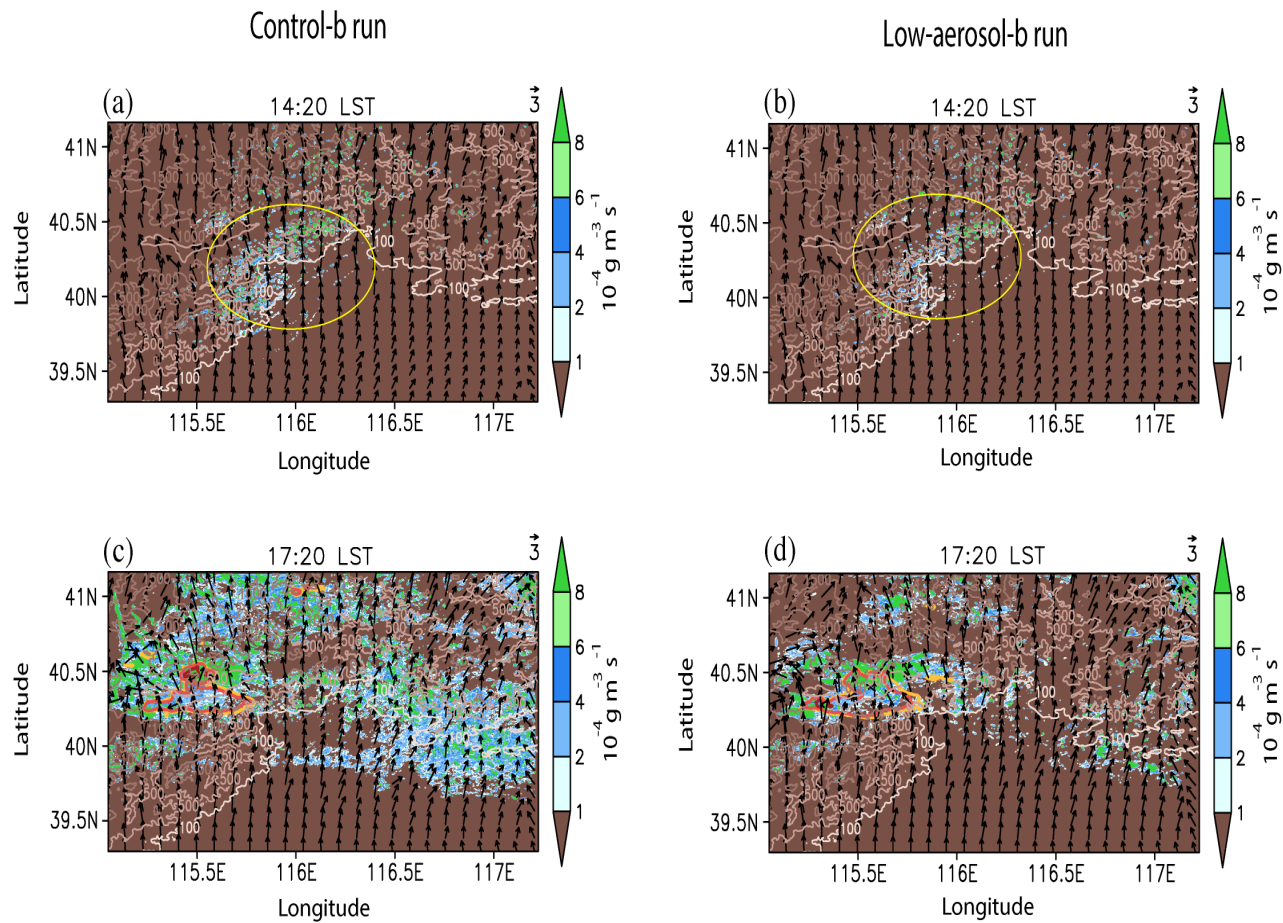


Figure 10

1289

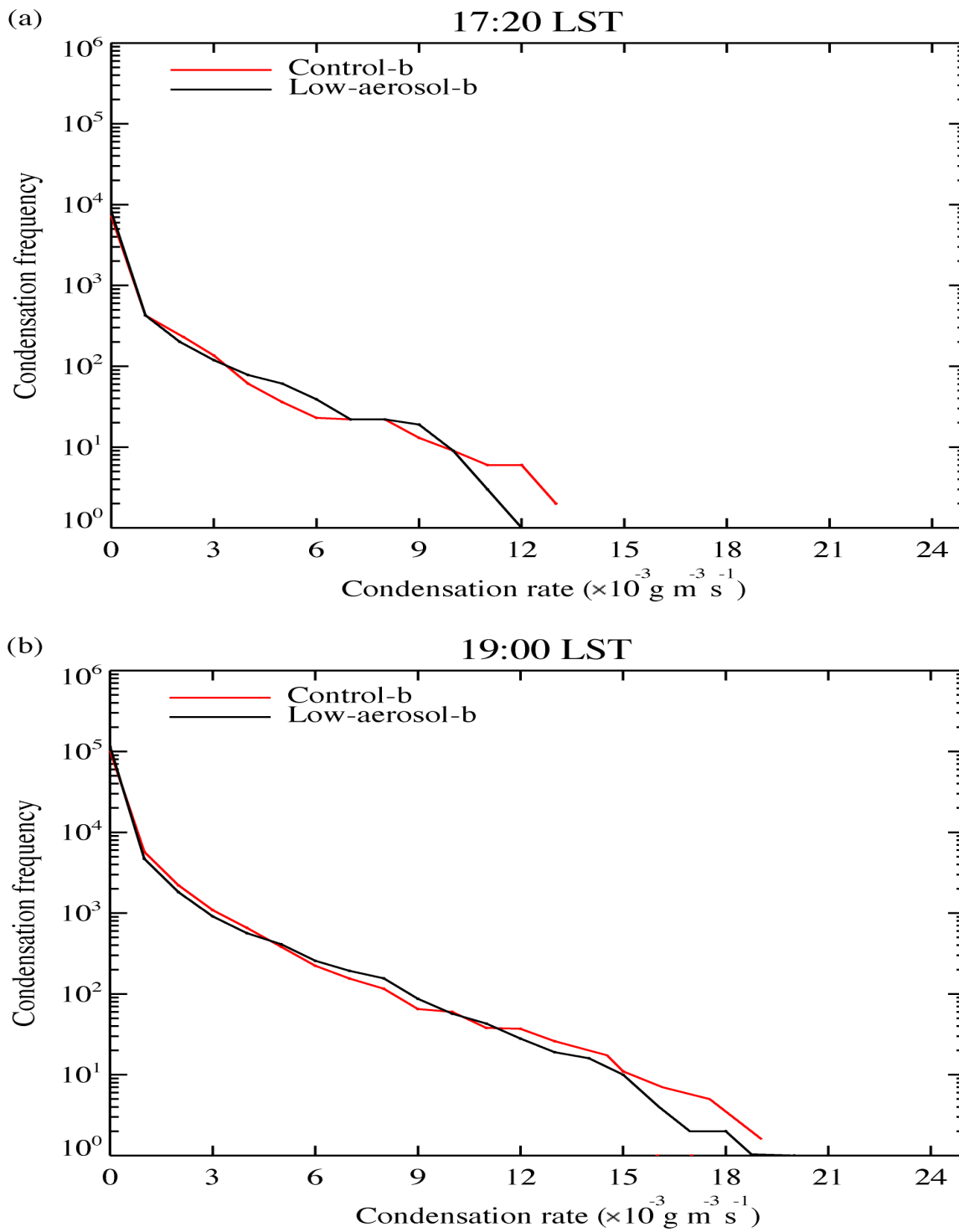
1290



1291
 1292
 1293
 1294
 1295

Figure 11

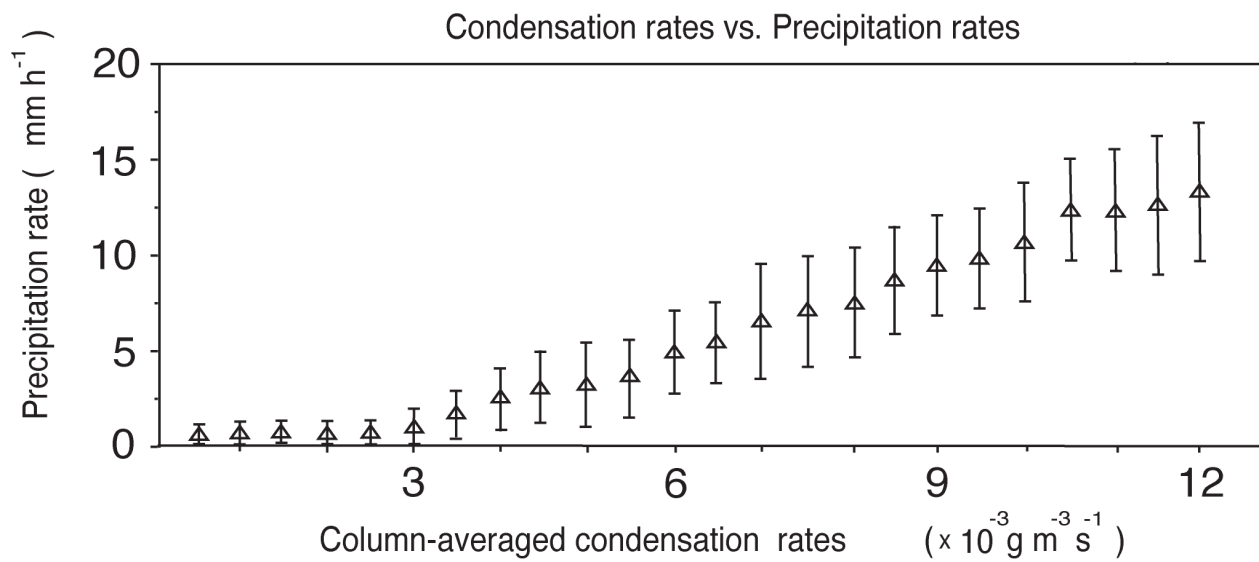
Beijing case



1296

1297

Figure 12



1298

1299

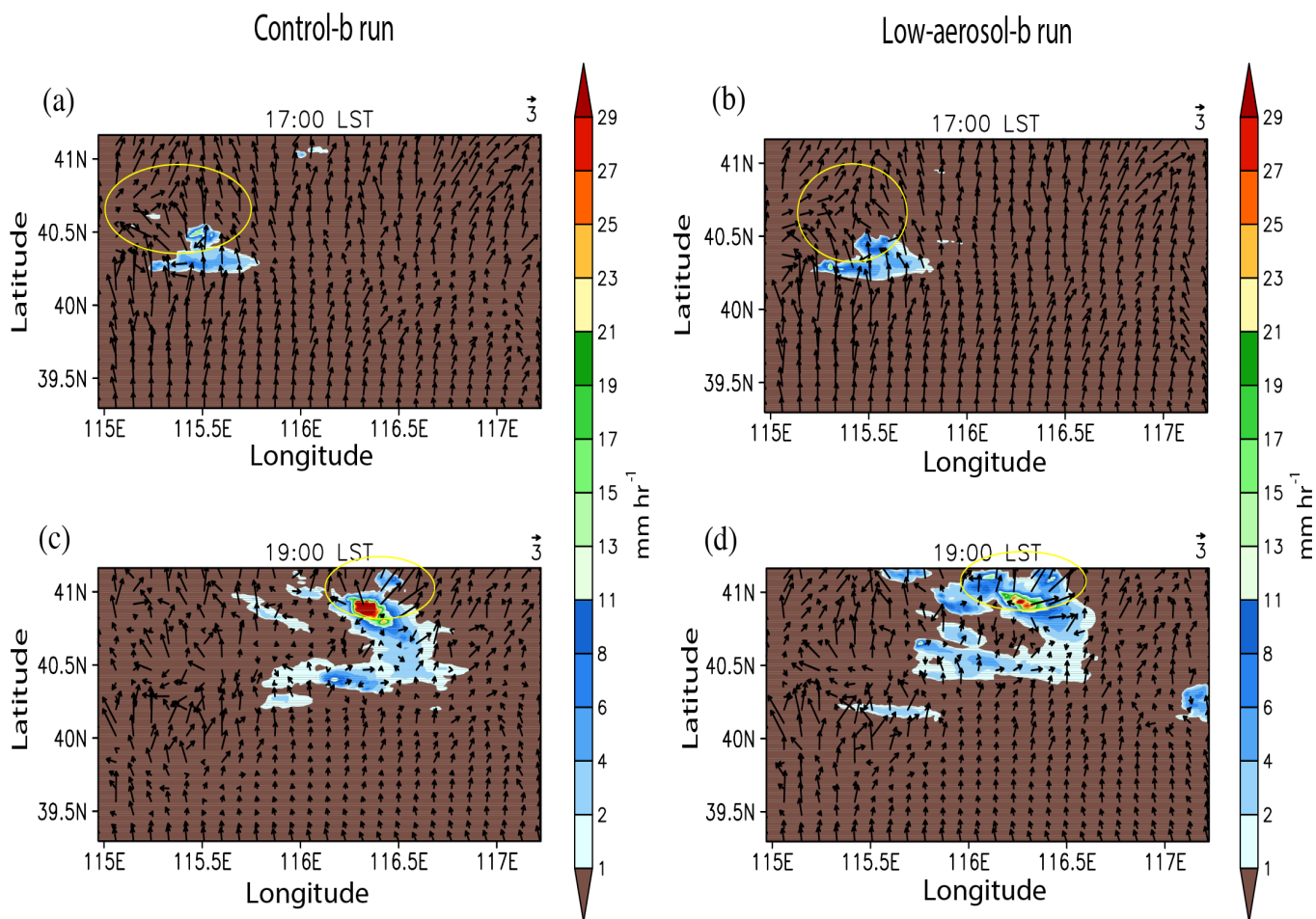
Figure 13

1300

1301

1302

1303



1304

1305

1306

1307

Figure 14